April 28, 2006

Tokai-to-Kamioka (T2K) Long Baseline Neutrino Oscillation Experiment Proposal

Executive Summary

In this document, we propose to construct a neutrino beam facility, using the fast extracted proton beam from J-PARC proton synchrotron in Tokai and to perform a long baseline neutrino oscillation experiment, using existing Super-Kamiokande detector (T2K experiment). This experiment is an international collaboration of Japan, Canada, France, Italy, Korea, Poland, Russia, Spain, UK and USA. Budget request of each country has been submitted to each financial agency.

This proposal is the first stage of the physics program. The feasibility of the future neutrino program depends on the results of this first stage, especially on the result of $\nu_\mu \to \nu_e$ search.

The goal of the T2K experiment

We request total integrated beam power larger than 0.75 MW x 15000h at any proton energies between 30 and 50 GeV. Since one year run with full beam power will probe physics by unprecedented sensitivities, it is possible that new finding occur any time. Even if we do not see new phenomena, every yearly run will produce meaningful upper limit. Thus it is critical to increase the beam power as soon as possible after commissioning of accelerator complex. The experiment has three main well defined goals.

1. The discovery of $\nu_\mu \to \nu_e$
   A factor of 20 improvement in sensitivity over the present upper limit is possible. The goal is to extend the search down to $\sin^2 2\theta_{13} \simeq 2\sin^2 2\theta_{\mu e} > 0.008$. The ν_e appearance measurement is important for two reasons.

   - The mixing angle θ_{13} is the last of the mixing angles in three neutrino scheme. We already know that other two mixing are large. One of the most interesting question is whether the third mixing angle is at same order of magnitude or small by many order of magnitudes. The observation of $\nu_\mu \to \nu_e$ in the first stage of the experiment prove that θ_{13} is not extremely small, so that a future CP violation search become practical.
   - This is an appearance channel and has a sub-leading oscillation of ν_μ involving Δm^2_{13}. The new developments in solar and reactor neutrino experiments indicate that ν_μ will oscillate to ν_e with a rather large mixing angle and Δm^2_{12}. This oscillation can compete with the one with a mass squared difference of Δm^2_{13}. The former oscillation is suppressed by a small Δm^2 and the latter is suppressed by the small mixing angle, θ_{13}. Hence, the two processes can compete. This is one of the necessary conditions for a CP violation effect to be observable.

2. The precision measurements of oscillation parameters in ν_μ disappearance
   Observation of the oscillation minimum, a 1% measurement (about the same precision as Cabbibo angle in quark sector) of the mixing angle and a 3% measurement of Δm^2 ($\delta(\Delta m^2_{23}) = 10^{-4}$ eV^2 and $\delta(\sin^2 2\theta_{23}) = 0.01$), may show the mixing of second and third generation neutrinos to be consistent with maximal at 1% accuracy. This may impose a constraint on the quark-lepton unification in the future.

3. Search for sterile components in ν_μ disappearance by detecting the neutral-current events
   If a non-zero sterile component is found, the physics of fermions will need modification to accommodate extra member(s) of leptons.

Feature of the T2K experiment

Needless to say, it is important to look for unexpected phenomena as well with new sensitivity. The neutrino beam has been designed with emphasis on the neutrino energy determination and on the flavor identification, taking into account the characteristics of Super-Kamiokande detector.

- The far detector
  T2K will use the world largest water Cherenkov detector, Super-Kamiokande (SK), as the far detector. Super-Kamiokande has excellent energy resolution and e/μ identification capability in low energy neutrino reactions, backed by about twenty years of experience of water Cherenkov detector.

- The neutrino beam energy
  The maximum sensitivity of the oscillation parameters can be achieved by tuning the neutrino beam energy to the oscillation maximum. The oscillation maximum will occur at a neutrino energy, E_ν, less than 1 GeV for the 295 km baseline with $\Delta m^2 \sim 3 \times 10^{-3} eV^2$. This neutrino energy is well matched to the detector capability.

- E_ν reconstruction
  The charged current interaction is dominated by the quasi-elastic interaction (CCQE) below 1 GeV. This enable us to make a precision determination of the neutrino energy of both ν_μ and ν_e. The energy can be calculated by a formula:

$$E_\nu = \frac{m_N E_l - m_l^2/2}{m_N - E_l + p_l cos\theta_l}, \quad (1)$$

  where m_N and m_l are the masses of the neutron and lepton (=e or μ), E_l, p_l and θ_l are the energy, momentum, and angle of the lepton relative to the neutrino beam, respectively.

- Off-axis beam
  The precision of the measurements are limited mainly due to the background events from high-energy components. The inelastic reactions of high-energy neutrinos constitute the backgrounds to neutrino energy measurements with the CCQE. In addition, the inelastic reactions produce π^0s that are the main background for ν_e appearance search. The experiment will use an off-axis beam to accomplish the highest possible intensity of low energy neutrinos with only a small high-energy tail in the spectrum.

- Start up of the experiment
  SK has been in operation for many years and the relevant software already exists. The intensity of the low energy neutrino beam is proportional to the proton beam power and does not require a specific proton energy in the initial operation of the accelerator. The experiment will be able to accommodate any reasonable start-up scenario of the accelerator, and can produce physics results in a short time after initial operation.

Japan

KEK
Y. Ajima, O. Araoka, Y. Fujii, K. Hayashi, N. Higashi, A. K. Ichikawa, T. Ishida, T. Ishii, K. Kasami, N. Kimura, T. Kobayashi, S. Koike, Y. Makida, T. Nakadaira, T. Nakamoto, K. Nakamura, K. Nishikawa*, T. Ogitsu, H. Ohhata, T. Okamura, Y. Oyama, K. Sasaki, K. Sakashita, T. Sekiguchi, S. Suzuki, M. Tada, K. Tanaka, M. Tanaka, A. Terashima, T. Tomaru, T. Tsukamoto, Y. Yamada, H. Yamaoka

ICRR, University of Tokyo
T. Abe, Y. Hayato, Y. Itow, J. Kameda, Y. Koshio, M. Miura, S. Moriyama, M. Nakahata, Y. Obayashi, H. Sekiya, M. Shiozawa, Y. Suzuki, A .Takeda, Y. Takeuchi

RCCN, University of Tokyo
I. Higuchi, T. Kajita, K. Kaneyuki, S. Nakayama, K. Okumura, C. Saji

Hiroshima University
T. Takahashi

Kobe University
S. Aoki, T. Hara, A. Suzuki

Kyoto University
T. Nakaya, H. Tanaka, M. Yokoyama

Tohoku University
T. Hasegawa

University of Tokyo
T. Abe, H. Aihara, M. Iwasaki, H. Kakuno, N. Hastings

Canada

TRIUMF
P. Amaudruz, M. Barnes, E. Blackmore, S. Chen, H. Coombes, J. Doornbos, W. Faszer, P. Gumplinger, R. Helmer, R. Henderson, I. Kato, P. Kitching, A. Konaka, L. Kurchaninov, G. Marshall, J. Macdonald, A. Miller, K. Olchanski, R. Openshaw, J.M. Poutissou, R. Poutissou, F. Retiere, P. Vincent, G. Wait, S. Yen,

University of Alberta
J.P. Archambault, J. McDonald, M.G Vincter

University of British Columbia
M. Bryant, J. Coulombe, C. Hearty, S. Oser, J. Wendland

University of Regina
T. Mathie, R. Tacik

University of Toronto
J. Martin

University of Victoria
P. Birney, A. Dowling, K. Fransham, C. Hansen, D. Karlen, R. Langstaff, M. Lenckowski, P. Poffenberger, M. Roney

York University
S. Bhadra

* T2K Contact person: Koichiro Nishikawa, Email address : nishikaw@neutrino.kek.jp

France

CEA SACLAY - DSM/DAPNIA - Service de Physique des particules
J. Argyriades, P. Baron, J. Bouchez, D. Calvet, Ch. Cavata, P. Colas, E. Delagnes, A. Delbart, F. Druillole, M. Fechner, A. Giganon, Y. Giomataris, J. Mallet, J.-Ph. Mols, L. Mosca, F. Pierre, A. Sarrat, M. Zito

LPNHE-IN2P3 Paris
J. Dumarchez

Italy

INFN - Sezione di Bari
M.G. Catanesi, E. Radicioni

INFN - University of Napoli
G. De Rosa, V. Palladino

INFN - University of Padova
M. Mezzetto, M. Laveder

INFN - University of Roma
U. Dore, C. Gargiulo, P.F. Loverre, L. Ludovici, C. Mariani

University of Ljubljana
T. Podobnik

Unversity of Naples Federico II G. De Rosa

Korea

Chonnam Naitonal University
J.Y. Kim, I.T. Lim

Dongshin University
M.Y. Pac

Kyungpook National University
W. Kim, V. Batourine

Kangwon University
S.K. Nam

KyungSang National University
I.G. Park

Sejong University
Y.D. Kim

Seoul National University
S. Choi, E.J. Jeon, K.K. Joo, S.B. Kim

SungKyunKwan University
Y.I. Choi, C.W. Park

Yonsei University
Y. Kwon

Gyeongsang National University
I.G. Park

Poland

Warsaw University
D. Kielczewska

Russia

Institute for Nuclear Research RAS
A.V. Butkevich, M. Khabibullin, A. Khotjantsev, Yu.G. Kudenko, B. Lubsandorjiev, V.A. Matveev, S.P. Mikheyev, O. Mineev, Y. Mussienko, N. Yershov
ITEP
M. Danilov, V. Balagura

Spain

University of Barcelona
J.L. Alcaraz, S. Andringa, X. Espinal, E. Fernández, F. Sánchez, T. Lux
University of Valencia
J. Burguet, J. Catala, A. Cervera-Villanueva, E. Couce, P.N Garijo, J.J. Gomez-Cadenas, P. Novella, M. Sorel, A. Tornero

Switzerland

ETH/Zurich
A. Rubbia
University of Geneva
A. Blondel, P. Bene, A. Cervera, D. Ferrere, F. Masciocchi, E. Perrin, R. Schroeter

UK

Imperial College London
S. Boyd, P. Dornan, G. Hall, M. Raymond, I. Taylor, Y. Uchida, A. Vacheret, F. van Schalkwyk, D.L. Wark
Lancaster University
I. Bertram, L. Kormos, P. Ratoff
University of Liverpool
C. Chavez, J. Fry, R. Gamet, D. Payne, P. Sutcliffe, C. Touramanis
Queen Mary Westfield College London
F.Di Lodovico, C.M. Cormack, R.A. Owen, A. Poll, C. Williams
Rutherford Appleton laboratory
A. Belias, J. Butterworth, S. Canfer, C. Densham, R. Edgecock, M. French, R. Halsall, J. Hirst, P. Loveredge, T.C. Nicholls, D. Morrow, G.F. Pearce, A. Weber, M. Woodward
University of Sheffield
C.N. Booth, S.L. Cartwright, R. French, E.V. Korolkova, M.L. Navin, L.F. Thompson
University of Warwick
J. Back, G.J. Barker, R. Bridgland, P.F. Harrison, A. Lovejoy, B. Morgan, A. Sheffield, J.A. Thornby

USA

Argonne National Laboratory
M. Goodman
Boston University
E. Kearns, M.D. Litos, J.L. Stone, L.R. Sulak
Brookheaven National Laboratory
M. Goldhaber, M. Harrison, P. Wanderer
University of California, Berkeley and Lawrence Berkeley National Laboratory
K. M. Heeger, Kam-Biu Luk
University of California, Irvine
D. Casper, J.A. Dunmore, W.R. Kropp, S. Mine, C.G. Regis, C. Simon, M.B. Smy, H.W. Sobel, M.R. Vagins
University of Colorado
R.H. Nelson, J.B. Spitz, E. Zimmerman
Duke University
K. Scholberg, N. Tanimoto, C.W. Walter
California State University Dominguez Hills
K. Ganezer, J. Hill, W. Keig
University of Hawaii
J.G. Learned, S. Matsuno
Los Alamos National Laboratory
T.J. Haines
Louisiana State University
S.A Dazeley, T.M. Goon, R. Gould, S. Hatakeyama, T. Kutter, W.J. Metcalf, K. McBryde, R. Svoboda
The University of Pennsylvania
E.W. Beier
The University of Rochester
A. Bodek, R. Bradford, H. Budd, J. Chvojka, R. Flight, S. Manly, K. McFarland, J. Park, W. Sakumoto, J. Steinman, M. Zielinski
The State University of New York at Stony Brook
C.K. Jung, K. Kobayashi, G. Lopez, C. McGrew, A. Sarrat, L.P. Trung, L. Whitehead, C. Yanagisawa
University of Washington
E. Berns, R. Gran, R.J. Wilkes

Contents

Chapter 1

Physics Motivation

1.1 The Current Situation in Neutrino Oscillation Physics

Over the last 7 years neutrino physics has crossed a threshold in its basic understanding of the fundamental nature of neutrinos. Initial indications of an anomaly in the solar neutrino flux from the pioneering experiments of Ray Davis and his collaborators [1], and from the Kamiokande experiment [2]. Then these results were supported by measurements of the low-energy solar neutrino fluxes by the SAGE [3] and GALLEX [4] experiments. While the solar neutrino anomaly was under investigation, the Super-Kamiokande (SK) experiment showed a zenith-angle dependent suppression of ν_μ flux (atmospheric neutrino flux, arising from cosmic ray interactions with the atmosphere) which indicated that neutrinos have mass [5]. Recently the SNO [6] experiment has demonstrated that the solar neutrino anomaly is caused by neutrinos changing flavor, which was shown to be consistent with neutrino oscillations by the recent results from the KamLAND experiment [7]. Most recently results from the K2K long-baseline neutrino oscillation experiment [8] have shown that the atmospheric neutrino anomaly observed by Super-Kamiokande appears in experiments with a controlled neutrino beam as well. It has been established that the neutrino does oscillate and two Δm^2's exist.

Neutrino oscillations arise quite naturally in a neutrino mixing model which is described by a unitary 3x3 matrix (Maki-Nakagawa-Sakata [9] (MNS) matrix) that is defined by a product of three rotation matrices with three angles (θ_{12}, θ_{23}, and θ_{13}) and a complex phase (δ) as in the Cabibbo-Kobayashi-Maskawa matrix [10].

$$\begin{pmatrix} \nu_e \\ \nu_\mu \\ \nu_\tau \end{pmatrix} = \begin{bmatrix} \\ U_{\alpha i} \\ \\ \end{bmatrix} \begin{pmatrix} \nu_1 \\ \nu_2 \\ \nu_3 \end{pmatrix}, \tag{1.1}$$

$$U = \begin{pmatrix} 1 & 0 & 0 \\ 0 & C_{23} & S_{23} \\ 0 & -S_{23} & C_{23} \end{pmatrix} \begin{pmatrix} C_{13} & 0 & S_{13}e^{-i\delta} \\ 0 & 1 & 0 \\ -S_{13}e^{i\delta} & 0 & C_{13} \end{pmatrix} \begin{pmatrix} C_{12} & S_{12} & 0 \\ -S_{12} & C_{12} & 0 \\ 0 & 0 & 1 \end{pmatrix}, \tag{1.2}$$

where $\alpha = e,\ \mu,\ \tau$ are the flavor indices, i=1, 2, 3 are the indices of the mass eigenstates, S_{ij} (C_{ij}) stands for $\sin\theta_{ij}$ ($\cos\theta_{ij}$). Neutrinos are produced as flavor eigenstates and each component of mass eigenstate gets a different phase after traveling a certain distance. The detection of neutrinos by charged current interactions projects these new states back onto flavor eigenstates.

For the simplest case, where only two of the mass states dominate the oscillations, the familiar formula which governs the appearance of one flavor, say ν_e, in an initially pure beam of another flavor, say ν_μ, can be derived:

$$P(\nu_\mu \to \nu_e) = \sin^2 2\theta \ \sin^2\left(\frac{1.27\Delta m^2 L}{E}\right) \tag{1.3}$$

where θ is whichever of the angles is contributing to this particular mixing, L is the distance from the source to the detector, E is the energy of the neutrino, and $\Delta m^2 = m_j^2 - m_i^2$ is the difference in the

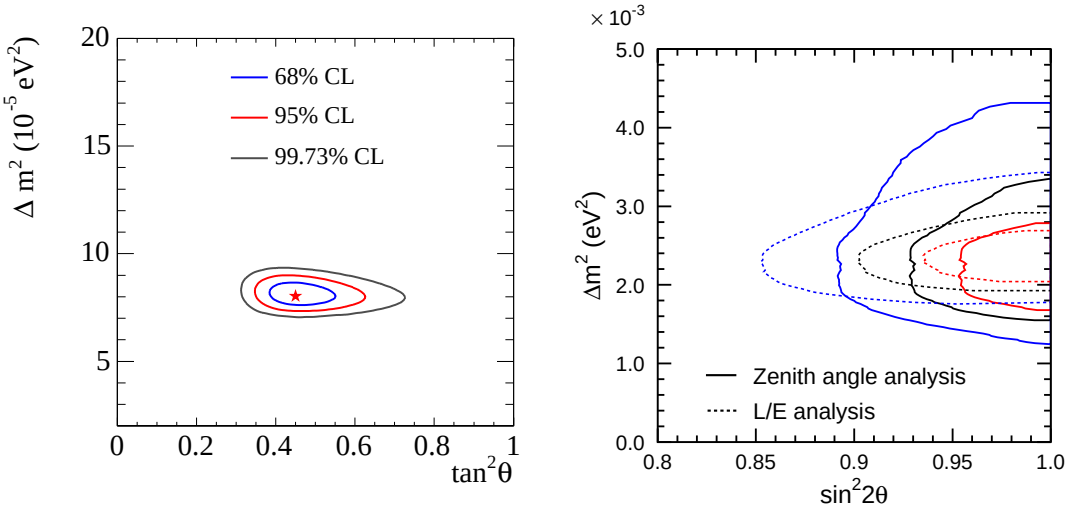

Figure 1.1: Allowed regions for 2-neutrino mixing parameters for solar+KamLAND (left figure) and from the latest Super-Kamiokande analysis (right figure). Note that the oscillations in the right figure are vacuum oscillations, and hence a plot in $\tan^2\theta$ would be symmetric about 1 (i.e., the sign of Δm^2_{23} is not determined).

squares of the masses of the two ν_i states that are mixing. The numerical constant 1.27 is valid for L in kilometers, E in GeV, and Δm^2 in eV^2. Note that these oscillations depend only on $|\Delta m^2|$, that is, they do not depend on either the absolute mass scale or ordering of the mass states. While this formula is valid in vacuum, interactions with electrons in matter can modify the oscillations [11]. It is called the matter effect which depends on the sign of Δm^2 and provides a way to determine the ordering of the mass states.

The current results for oscillations from solar neutrino plus KamLAND data can be fit using two-neutrino oscillations with the matter effect, and the resulting parameters are shown in the left part of Figure 1.1. Similarly, for the atmospheric oscillations the current best fit parameters from Super-Kamiokande are shown in the right part of Figure 1.1. These results constrain θ_{12}, θ_{23}, $|\Delta m^2_{23}|$ and the sign of Δm^2_{12}. It must be noted at this point that there is another claim of neutrino oscillations currently in the literature — that of the LSND collaboration [12]. They claim observation of $\overline{\nu}_\mu \rightarrow \overline{\nu}_e$ oscillations in a beam of $\overline{\nu}_\mu$ from stopped π decay. The KARMEN experiment [13], which had similar sensitivity, has failed to confirm these results, but has not completely excluded all of the range of parameters indicated by LSND. The Δm^2 value favored by the LSND claim is much larger (~ 1 eV^2) than that seen in solar or atmospheric neutrino oscillations. A new experiment (MiniBooNE [14]) at Fermilab is currently checking the LSND claim. If the LSND results are confirmed it will require a complete reevaluation of our current picture of neutrino oscillations, which cannot accommodate separate Δm^2 values with just three neutrinos. One of the goals of T2K includes a search for sterile ν by measuring neutral current events.

There are still three undetermined parameters in the MNS matrix — the angle θ_{13}, the sign of Δm^2_{23}, and the value of the CP-violating phase δ. These are fundamental parameters which should be predicted by a deeper theory of particle physics, and hence intrinsically interesting in themselves. It should be pointed out that measurements of the corresponding CKM parameters have been the focus of much of particle physics over the last three decades, and provided the physics justification for many facilities, including the current B factories at KEK and SLAC. The MNS matrix elements, due to the lack of hadronic corrections, can probably be determined to greater accuracy than can the CKM matrix elements, which have been the focus of so much determined effort. Another powerful

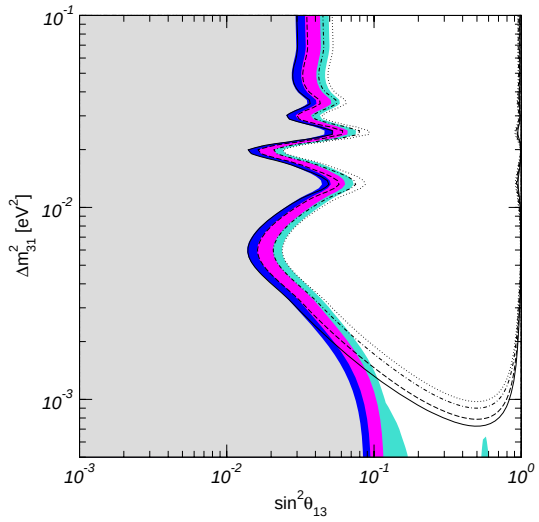

Figure 1.2: Allowed region for θ_{13} from CHOOZ alone (lines) and also including data from solar neutrino experiments and KamLAND (colored regions) at 90%, 95%, 99%, and 3σ. From Maltoni *et al*, hep-ph/0309130.

reason to pursue these studies is provided by the still unexplained matter-antimatter asymmetry of the present-day Universe. One possible source of the CP violation needed to explain this asymmetry is the neutrino sector, via the mechanism known as leptogenesis [15], and measuring the CP-violating phase δ in the MNS matrix should give valuable insight into the CP properties of neutrinos. However, as will be explained below, measuring δ is only possible if θ_{13} is sufficiently large, and hence a measurement of θ_{13} is critical step for future neutrino physics.

Our current knowledge of θ_{13} comes from three sources. Atmospheric and solar neutrino oscillation results give some information, but the most useful data for constraining the value of θ_{13} comes from the CHOOZ reactor $\bar{\nu}_e$ oscillation experiment [16]. This experiment measured the flux of $\bar{\nu}_e$ at a distance of 1 km from the CHOOZ reactor in France. Given the strong constraints on Δm^2_{13} arising from the other oscillation results we know that a suppression of this flux should have been seen if θ_{13} were large (like the two other angles), and therefore we are able to constrain $\sin^2\theta_{13}$ to be less than $\sim 6 \times 10^{-2}$ at the 90% C.L. in the region of Δm^2_{13} indicated by Super-Kamiokande (see Figure 1.2).

1.2 Future Progress in Neutrino Oscillation Physics

In addition to the MiniBooNE experiment mentioned above, the next few years should see the beginning of data taking by two long baseline oscillation programs — the NuMI neutrino beam from Fermilab [17], which is aimed at the MINOS detector 735 kilometers away in the Soudan mine; and the CNGS neutrino beam from CERN, which is aimed at the Laboratori Nazionali del Gran Sasso (LNGS) in Italy, where two experiments (OPERA [18] and ICARUS [19]) are currently under construction. The MINOS detector will make sensitive measurements of muon neutrino disappearance*, and thereby make a measurement of Δm^2_{23} accurate to about 10%. The CNGS experiments are using a higher-energy neutrino beam, and are aimed at making a conclusive demonstration of the mechanism for atmospheric neutrino disappearance by actually observing the appearance of ν_τ from $\nu_\mu \rightarrow \nu_\tau$ oscillations.

The next goal would then be to improve our sensitivity to θ_{13} in the hope of a positive observation. Our current knowledge of neutrino oscillations tells us that all neutrino oscillations observable on the Earth will be dominated by the two oscillations measured with solar and atmospheric neutrinos, and that any θ_{13} experiment must therefore look to small corrections to these oscillations caused by the

* recently the first results were presented[20]

sub-dominant effects which are all that θ_{13} will give rise to (given that we already know that θ_{13} is small). To understand these sub-dominant effects we need to go beyond the 2-neutrino formula shown above and look at the oscillation formula taking into account the full 3-neutrino mixing matrix:

$$\begin{aligned} P(\nu_\mu \to \nu_e) = & \quad 4C_{13}^2 S_{13}^2 S_{23}^2 \sin^2\ \Phi_{31} \times \left(1 + \tfrac{2a}{\Delta m_{31}^2}(1 - 2S_{13}^2)\right) \\ + & \quad 8C_{13}^2 S_{12} S_{13} S_{23}(C_{12} C_{23} \cos\ \delta - S_{12} S_{13} S_{23}) \cos\ \Phi_{32} \cdot \sin\ \Phi_{31} \cdot \sin\ \Phi_{21} \\ - & \quad 8C_{13}^2 C_{12} C_{23} S_{12} S_{13} S_{23} \sin\ \delta \cdot \sin\ \Phi_{32} \cdot \sin\ \Phi_{31} \cdot \sin\ \Phi_{21} \\ + & \quad 4S_{12}^2 C_{13}^2 \left(C_{12}^2 C_{23}^2 + S_{12}^2 S_{23}^2 S_{13}^2 - 2C_{12} C_{23} S_{12} S_{23} S_{13} \cos\ \delta\right) \sin^2\ \Phi_{21} \\ - & \quad 8C_{13}^2 S_{13}^2 S_{23}^2 \left(1 - 2S_{13}^2\right) \tfrac{aL}{4E_\nu} \cos\ \Phi_{32} \cdot \sin\ \Phi_{31}. \end{aligned} \tag{1.4}$$

Here, $\Phi_{ij} \equiv \Delta m_{ij}^2 L/4E$. This expression is complex, and even this is only an approximation (the matter effects come in through the terms multiplied by the parameter a, which depends upon the electron density, fundamental constants and mass differences, and in this formula the matter effects are calculated in the approximation of constant density). Analyzing the predictions of this formula is currently rather difficult, as it contains three unknown quantities (δ, θ_{13}, and the sign of Δm_{23}^2, which comes into the matter effect parameter a), as well as all the other oscillation constants, which of course have uncertainties in their measured values. However given the already known limits on the parameters it is possible to produce an approximate form of this formula that makes the point of the T2K experiment a little easier to explain:

$$\begin{aligned} P(\nu_\mu \to \nu_e) \ \approx & \ \sin^2 2\theta_{13} \sin^2 2\theta_{23} \sin^2 \Delta \\ \pm & \ \alpha \sin 2\theta_{13} \sin\delta \cos\theta_{13} \sin 2\theta_{12} \sin 2\theta_{23} \sin^3 \Delta \\ - & \ \alpha \sin 2\theta_{13} \cos\delta \cos\theta_{13} \sin 2\theta_{12} \sin 2\theta_{23} \cos\Delta \sin 2\Delta \\ + & \ \alpha^2 \cos^2\theta_{23} \sin^2 2\theta_{12} \sin^2 \Delta \end{aligned}$$

where $\alpha \equiv \Delta m_{21}^2/\Delta m_{31}^2$ and $\Delta = \Delta m_{31}^2 L/4E$. The existing limits from joint fits to the solar, KamLAND, and Super-K atmospheric data show that $\alpha \approx 3 \times 10^{-2}$. CHOOZ + solar neutrino data shows that $\sin^2 2\theta_{13} <\sim 0.2$, and of course the value of δ is completely unknown. For the values which will be used in the T2K experiment all the other terms in this expansion are ~ 1. It should also be noted that this expansion sets the matter terms to zero, however for T2K that is an excellent approximation. Looking at the approximate formula, the only term that doesn't depend on θ_{13} is the last one (which is in fact the approximate form for the oscillations that KamLAND sees), but this depends on α^2 and is therefore unobservable in T2K. For values of $\sin 2\theta_{13}$ within an order of magnitude of its current upper limit, the first term dominates, which describes a relatively simple oscillatory appearance of ν_e in ν_μ beam.

That then suggests the proper target for future experiments. Firstly, we need to improve our sensitivity to θ_{13} by at least an order of magnitude, and hopefully more. The MINOS and the CNGS experiments should produce some improvement in our sensitivity, but certainly not an order of magnitude. At the same time measuring θ_{23} and Δm_{23}^2 with greater precision is interesting in its own right (in particular, the deviation of θ_{23} from $\pi/4$ is a matter of great interest to model builders) as well as being a necessary for extracting the values of the so-far unmeasured parameters from oscillation measurements.

1.3 The T2K Long Baseline Experiment

The first phase of the T2K experiment is therefore aimed at three main goals — the more accurate determination of the "atmospheric" parameters θ_{23} and Δm_{23}^2, a measurement of θ_{13} with more than an order of magnitude sensitivity than any previous experiments, and a search for $\nu_\mu \to \nu_\tau$ component. The project is based on adding a beam line (of which more detail is described in the chapter 2) to

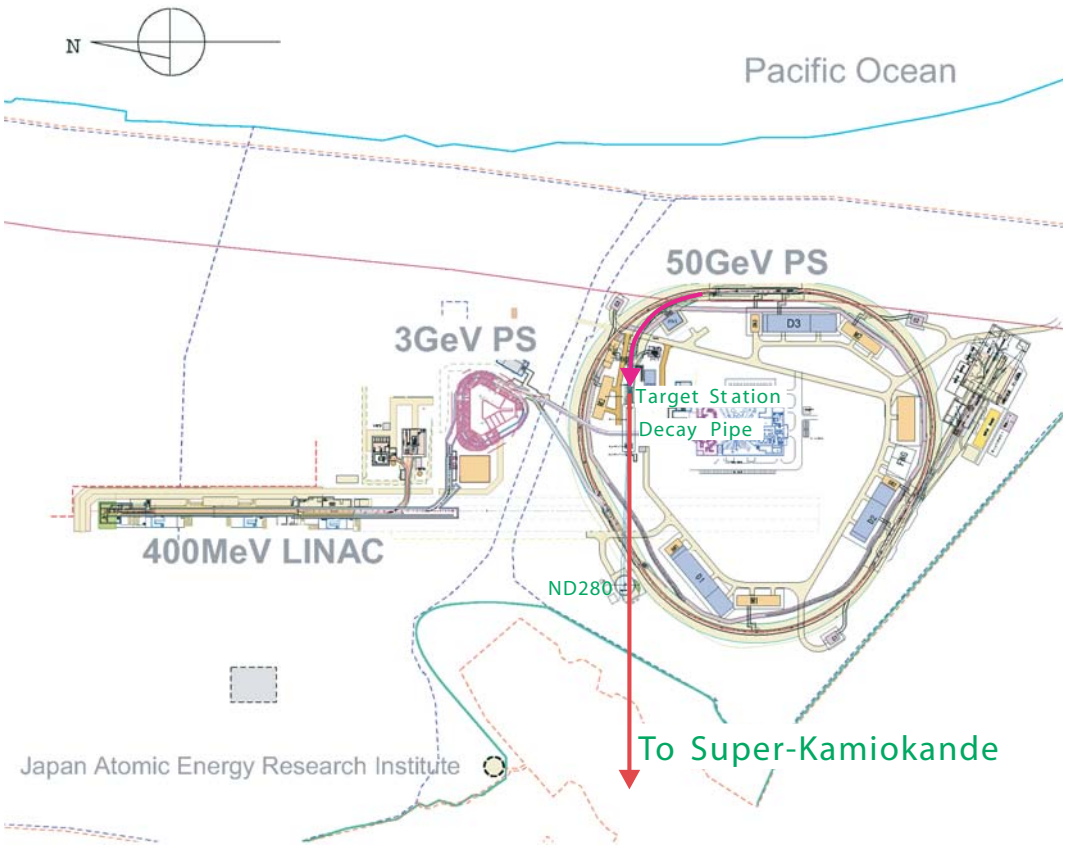

Figure 1.3: Overview of the J-PARC facility.

redirect the proton beam from the 50 GeV synchrotron currently under construction at the new J-PARC facility (Figure 1.3) in Tokai, Japan [21] to produce an intense neutrino beam. The high power of the J-PARC proton beam, 0.75 MW in Phase-I, will produce the most intense neutrino beam ever built. We request total integrated beam power larger than 0.75 MW x 15000h at any proton energies between 30 and 50 GeV. Operation of 0.75 MW with 50GeV beam energy can deliver 10^{21} POT with 3000h run time. We assume 10^{21} POT with 40GeV beam energy for the studies shown in this proposal. Since the lower energy operation of accelerator with the same beam power 0.75 MW can deliver more neutrinos as described in the subsection 1.5, the results in this document are conservative.

A set of detectors are located 280 m from the pion production target to characterize the neutrino beam. This beam then propagates underground for 295 km to the Super-Kamiokande (SK) detector [22] in western Japan, which is well suited for distinguishing ν_μ and ν_e in the neutrino beam by looking at Cherenkov radiation from μ's and e's produced by charged-current interactions in its 50 kton water target. A key element of the design of the T2K facility is that the neutrino beam is directed so that the beam axis actually misses Super-Kamiokande (off-axis neutrino beams). This, rather surprisingly, actually results in a considerable improvement in the quality of the beam for the ν_e appearance experiment. This arises from the kinematics of π decay, which result in an enhancement in the neutrino flux produced over a very narrow range of energies which depend on the exact off-axis angle (see Figure 1.4). By selecting the correct angle, this narrow peak can be near on the oscillation maximum at the far detector, SK. This has three major advantages over a conventional on-axis beam. Firstly, the off-axis neutrino flux at the desired energy (near the oscillation maximum) is actually higher than on-axis. Secondly, there are fewer high-energy neutrinos, which do not contribute to the appearance signal but do contribute to its backgrounds, in particular through the neutral-current production of π^0's (which decay to produce two γ's, which can sometimes be mistaken for the single electron characteristic of a charged-current interaction with a ν_e). Thirdly, the background due to the intrinsic contamination of the beam by ν_e is actually less at the off-axis position due to the different

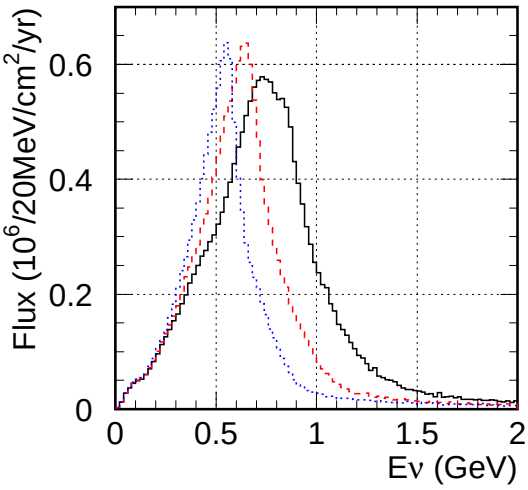

Figure 1.4: Energy spectra from off-axis beams: black-solid line (2 degree), red-dashed line (2.5 degree), and blue-dotted line (3 degree). As the off-axis angle increases, the energy peak narrows and moves lower in energy.

kinematics of the decays that lead to ν_e.

The very kinematics that give a useful selection in energy, however, mean that the characteristics of the beam change rapidly with angle. Detailed measurement of the beam properties will therefore be required to minimize the systematic uncertainties in any neutrino oscillation measurement. These detailed measurements will be made with a set of near detectors at 280 m downstream of the target.

1.4 T2K physics goals

The main physics goals of the T2K experiment are:

- A precision measurement of the neutrino oscillation parameters, $(\sin^2 2\theta_{23}, \Delta m^2_{23})$, by the measurement of ν_μ disappearance.
- The determination of $\sin^2 2\theta_{13}$ by the measurement of the $\nu_\mu \rightarrow \nu_e$ appearance signal.
- Search for $\nu_\mu \rightarrow \nu_\tau$ component of oscillation by the measurement of neutral current events.

1.4.1 ν_μ disappearance

The neutrino oscillation parameters, $(\sin^2 2\theta_{23}, \Delta m^2_{23})$, will be determined by measuring the survival probability of ν_μ after traveling 295 km. Neutrino events in SK are selected as fully-contained events with visible energy ($E_{vis.}$) greater than 30 MeV in the fiducial volume of 22.5 kton. The events are further selected by requiring the presence of a single muon-like ring. The expected number of events without oscillation for an off-axis angle of 2.5° and 5×10^{21} protons on target (POT) are summarized in Table 1.1. The numbers of events after oscillation as a function of Δm^2_{23} are shown in Table 1.2 for the values of oscillation parameters $\sin^2 2\theta_{23} = 1.0$ and $\sin^2 2\theta_{13} = 0.0$.

In order to measure the oscillation parameters, the neutrino energy distribution of the fully-contained single ring μ-like events is reconstructed using an extended-maximum likelihood method. The reconstructed neutrino energy distribution and the ratio of the prediction with the best-fit oscillation parameters (from existing experiments) to the prediction without oscillations is shown in Figure 1.5. The expected statistical uncertainty on the measurements is 0.009 for $\sin^2 2\theta_{23}$ and $5 \times 10^{-5}\mathrm{eV}^2$ for Δm^2_{23}, and is shown as a function of the true Δm^2_{23} in Figure 1.6.

We have studied the effects of the following systematic uncertainties.

	CC-QE	CC-nonQE	NC	All ν_μ
Generated in FV	4,114	3,737	3,149	11,000
(1) FCFV	3,885	3,011	1,369	8,265
(2) $E_{vis.} \geq 30$ MeV	3,788	2,820	945	7,553
(3) Single ring μ-like	3,620	1,089	96	4,805

Table 1.1: The expected number of neutrino events for 5×10^{21} POT for ν_μ disappearance analysis without oscillation. CC-QE refers to charged current quasi-elastic events and CC-nonQE to other charged current events, while NC refers to neutral current events.

Δm^2 (eV^2)	CC-QE	CC-nonQE	NC	All ν_μ
No oscillation	3,620	1,089	96	4,805
2.0×10^{-3}	933	607	96	1,636
2.3×10^{-3}	723	525	96	1,344
2.7×10^{-3}	681	446	96	1,223
3.0×10^{-3}	800	414	96	1,310

Table 1.2: The expected number of neutrino events for 5×10^{21} POT for ν_μ disappearance analysis with neutrino oscillation for different values of Δm^2_{23} with $\sin^2 2\theta_{23} = 1.0$ and $\sin^2 2\theta_{13} = 0.0$.

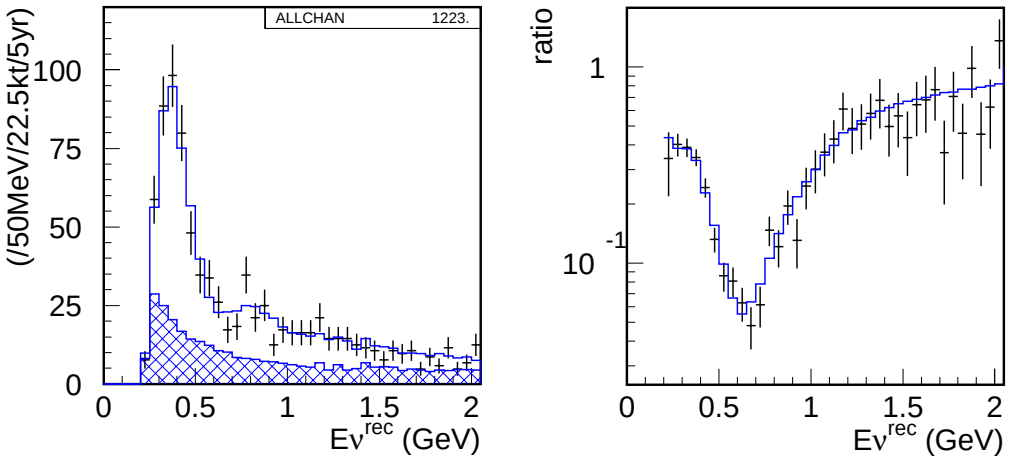

Figure 1.5: (Left) The reconstructed neutrino energy distribution with predicted for the best-fit oscillation parameters $(\sin^2 2\theta_{23}, \Delta m^2_{23}) = (1.0, 2.7 \times 10^{-3}\text{eV}^2)$. The hatched area shows the non-QE component. (Right) The ratio of the reconstructed neutrino energy distribution with oscillation to one without oscillation.

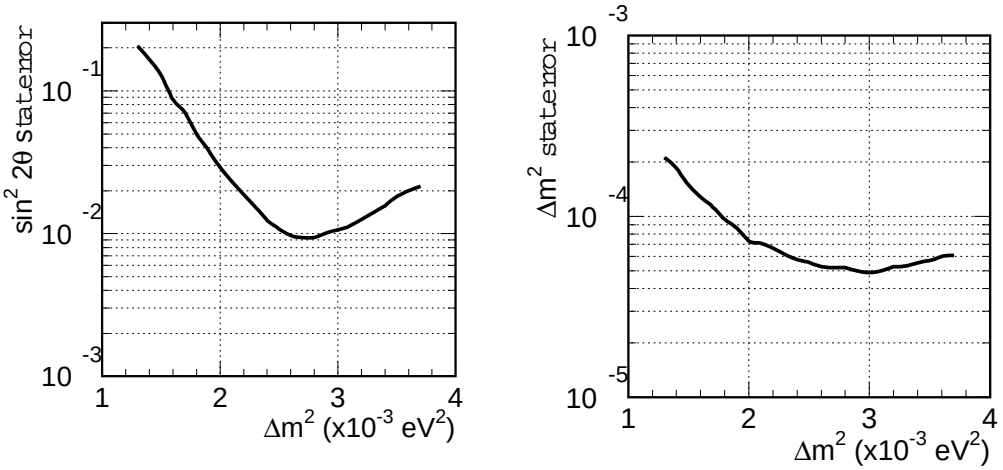

Figure 1.6: The statistical uncertainty of the oscillation parameters as a function of true Δm^2_{23}. The value of $\sin^2 2\theta_{23}$ is assumed to be one.

1. The uncertainty in the predicted number of the fully-contained single ring μ-like events. We consider 10 % uncertainty (Red curve).
2. The uncertainty in the non-QE/QE ratio. We consider 20 % uncertainty (Green).
3. The uncertainty in the energy scale. We consider 4 % uncertainty (Blue).
4. The uncertainty in the spectrum shape (Pink). We multiply a weighting factor $1+0.2(1-E_\nu)+const.$ to neutrino spectrum. This change roughly represents the difference of spectra predicted by MARS and FLUKA hadron production models.
5. The uncertainty in the spectrum width (Lightblue). We consider 10% uncertainty.

Figure 1.7 shows the effect of the systematic errors. In order to keep the systematic uncertainties below the statistical error, the uncertainties should be less than about 5 % for the predicted number of events, 2 % for the energy scale, and 5-10 % for the non-QE/QE ratio, 10% for the spectrum width. The spectrum shape uncertainty should be less than the difference of the hadron production models MARS and FLUKA.

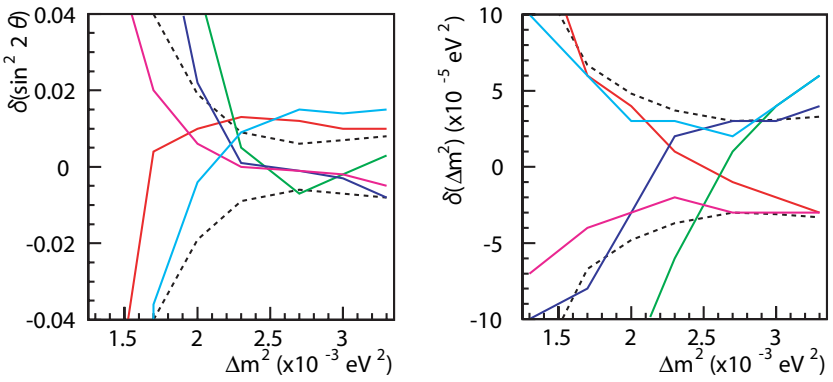

Figure 1.7: Effects of systematic uncertainties on determination of oscillation parameters (OA2.5deg). Red curve: the effect when flux is changed by 10%, Green: nonQE/QE ratio changed by 20%, Blue: energy scale changed by 4%, Pink: spectrum shape (see text), Lightblue: width of spectrum changed by 10%. The dashed curve indicate 1σ statistical error.

	ν_μCC BG	ν_μNC BG	beam ν_e BG	ν_eCC signal
Fully-contained, E_{vis} $\geq$100MeV	2215	847	184	243
1 ring e-like, no decay-e	12	156	71	187
0.35$\leq E_\nu^{rec.} \leq$0.85GeV	1.8	47	21	146
e/π^0 separations	0.7	9	13	103

Table 1.3: The number of events selected by the ν_e appearance analysis, as predicted by NEUT Monte Carlo for 5×10^{21} POT exposure. For the calculation of oscillated ν_e, $\Delta m^2 = 2.5 \times 10^{-3}\mathrm{eV}^2$ and $\sin^2 2\theta_{13} = 0.1$ are assumed.

1.4.2 ν_e appearance

The ν_e selection cuts are based on the SK-1 atmospheric neutrino analysis. Events are required to be fully contained within the 22.5kton fiducial volume, have visible energy (E_{vis}) greater than 100MeV, a single electron like (e-like) ring, and no decay electrons. The electron identification eliminates the most muon background events, and the decay electron cut further reduces events from inelastic charged current (CC) processes associated with π^0 production. The dominant source of background events (see Table 1.3) at this stage is single π^0 production in neutral current (NC) interactions. The backgrounds can be further reduced by requiring the reconstructed neutrino energy to be around the oscillation maximum: 0.35 GeV $\leq E_\nu^{rec.} \leq$ 0.85GeV.

The remaining background from π^0 is further reduced with specific "e/π^0 separation" cuts. The π^0 background has a steep forward peak towards the neutrino direction due to coherent π^0 production. Thus events in the extreme forward direction ($\cos\theta_{\nu_e} \geq 0.9$) are rejected. Then events with only one high-energy gamma detected in the asymmetric decay of the π^0 are the dominant background. In order to find the hidden lower-energy gamma ring, the photomultiplier hit pattern, including scattered light, is fit under the hypothesis of two gamma rings. The energy and direction of each gamma ring are reconstructed, and the invariant mass of two rings is calculated. The π^0 background is further suppressed by rejecting events with the mass at around the π^0 mass ($m_{2\gamma}^{rec.} \geq 100\mathrm{MeV/c}^2$). These further "e/$\pi^0$' separation' cuts significantly reduce the π^0 background. The background level due to NC-π^0 is expected to be comparable to the predicted background from intrinsic ν_e in the beam.

Table 1.3 summarizes the number of events after the event selections for 5×10^{21} POT exposure at $\Delta m^2 = 2.5 \times 10^{-3}\mathrm{eV}^2$ and $\sin^2 2\theta_{13} = 0.1$.

As a sensitivity, we calculate the 90% upper limit for an experiment that observes the expected background rate. Figure 1.8 shows the 90% C.L. ν_e sensitivity for 5×10^{21} POT exposure and for $\sin^2 2\theta_{23} = 1$ and $\delta = 0, \pi/2, -\pi/2, \pi$, assuming a 10% systematic uncertainty in the background subtraction. The sensitivity is $\sin^2 2\theta_{13} = 0.008$ at 90% C.L. for $\Delta m^2 \sim 2.5 \times 10^{-3}\mathrm{eV}^2$. This represents an order of magnitude improvement over the CHOOZ limit.

Figure 1.8 shows the 90% C.L. and 3σ ν_e sensitivities as a function of the exposure time for $\Delta m^2 = 2.5 \times 10^{-3}\mathrm{eV}^2$ for systematic uncertainties in the background subtraction of 5%, 10%, and 20%. This graph suggests the target for the near detectors of a 10% uncertainty in the background in the first phase (5×10^{21} POT = SK$\times$5years).

1.4.3 ν_τ versus $\nu_{sterile}$ analysis

The analysis of ν_τ appearance has been performed by the Super-Kamiokande collaboration [24]. This measurement disfavors a pure $\nu_\mu \rightarrow \nu_{sterile}$ solution to the atmospheric neutrino anomaly. The search for $\nu_\mu \rightarrow \nu_{sterile}$ with small mixing angle is still an interesting topic that can be addressed by the T2K experiment. The analysis method is based on the neutral current measurement in the SK detector, a clear signature of which is single π^0 production. The analysis is performed in a similar way to the previous ones:

- 22.5 kton fiducial volume cut is applied.

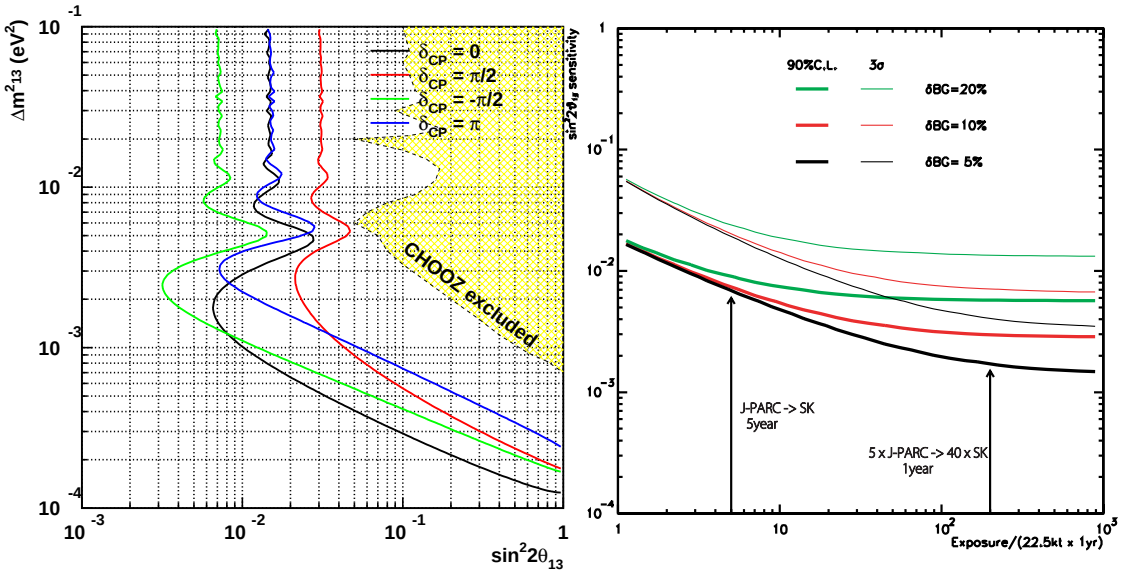

Figure 1.8: (Left) The 90% C.L. sensitivity to $\sin^2 2\theta_{13}$ for an exposure of 5×10^{21} POT with the assumption of maximum mixing, $\sin^2 2\theta_{23} = 1.0$, and the CP violation phase $\delta = 0, \pi/2, -\pi/2, \pi$. The 90% excluded region of CHOOZ is overlaid for comparison with $\sin^2 2\theta_{23} = 1.0$. (Right) The expected 90% C.L. and 3σ sensitivities of $\sin^2 2\theta_{13}$ as a function of exposure time (5 years $\equiv 5 \times 10^{21}$ POT) for three different uncertainties in background subtraction. We assume $\Delta m^2 = 2.5 \times 10^{-3}\mathrm{eV}^2$ and $\delta = 0$.

	ν_μ CC	$\nu_\mu + \nu_\tau$ NC $\nu_\mu -> \nu_\tau$	ν_μ NC $\nu_\mu -> \nu_s$	ν_e
Generated in Fiducial Volume	3,173	3,239	1,165	236
(1) 100 MeV $\leq E_{vis.} \leq$ 1500 MeV	184	724	429	109
(2) Two e-like rings	31	281	125	19
(3) No decay electron	9	255	104	14

Table 1.4: The expected number of neutrino events in 5×10^{21} POT for ν_τ appearance analysis without oscillation. The third and fourth columns show the comparison for the two cases where the oscillation is purely to ν_τ or to ν_s. The numbers are computed assuming $\sin^2 2\theta_{23} = 1.0$ and $\Delta m^2 = 2.7 \times 10^{-3}\mathrm{eV}^2$.

- The visible energy is selected between 100 MeV and 1500 MeV.
- Events are selected for 2 e-like rings.
- Events are selected with no decay electrons to further suppress the CC background.

The event suppression by the cuts is shown in Table 1.4. The purity of the final NC sample is 83%, with 255 total expected events for an exposure of 5×10^{21} POT.

The sensitivity to the fraction of ν_s in $\nu_\mu \rightarrow \nu_\tau$ oscillation is shown in Figure 1.9 as a function of Δm^2 and $\sin^2 2\theta_s$. The best limit, $\sin^2 2\theta_s \leq 0.2$, is obtained for $\Delta m^2 \approx 3 \times 10^{-3} eV^2$. The effect of systematic uncertainties is shown in Figure 1.9, where the sensitivity to $\sin^2 2\theta_s$ is plotted as a function of the exposure time for two values of systematic error on the NC prediction: 5% and 10%. A 10% error already dominates the measurement after the first year (10^{21} POT), and a value of the order of 5% improves the sensitivity by less than a factor of 2 at 5×10^{21} POT. The main systematic error for this analysis is knowledge of NC π^0 production, similar to the ν_e appearance analysis.

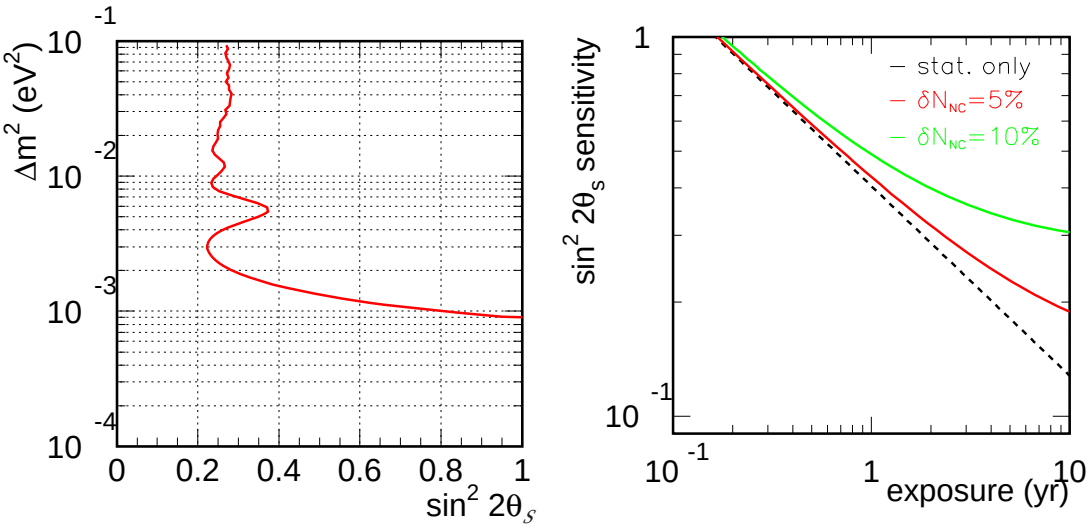

Figure 1.9: (Left) Sensitivity to the ν_s fraction in the $\sin^2 2\theta_s$ vs. Δm^2 plane with 5×10^{21} POT. (Right) The sensitivity as a function of exposure with different uncertainties in the background estimation.

1.5 Comparison of the primary proton beam energy

Figure 1.10 shows expected neutrino fluxes at various primary proton energies normalized to same total beam power. The spectrum shape is rather independent on the primary proton beam energy. The 30 GeV proton beam gives ∼10% higher neutrino flux than that of the 50 GeV proton beam assuming the same beam power. The higher energy tail in the flux, which produces background to the oscillation signal, is less at 30 GeV. Current physics sensitivity is dominated by statistics. Therefore, the first priority for the decision of the primary proton beam energy should be put on the total available beam power. If same power is available at any energy from 30 GeV to 50 GeV, the 30 GeV beam is more preferable for the T2K experiment because of its higher efficiency to produce neutrino flux and less high energy tail.

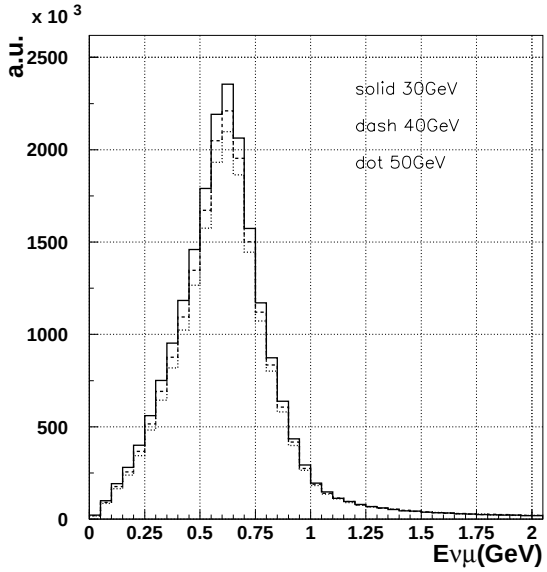

Figure 1.10: Comparison of neutrino flux at various primary proton energy with same total beam power. The off-axis angle is 2.5 degrees.

Chapter 2

Neutrino Beam

In this chapter, the neutrino beam line is described. After an overview, status and schedule of each component is reported.

2.1 Overview of the neutrino beamline

2.1.1 Neutrino beam production

A neutrino beam at J-PARC is produced with "conventional method" where pions produced by hitting protons on target decay into ν_μ and muons. The πs are focused by toroidal magnets called the electromagnetic horns and injected into a volume where they decay in flight (decay volume). The beam is almost pure ν_μ. The sign of ν_μ or $\bar{\nu}_\mu$ can be selected by flipping the polarity of the horns.

In the T2K experiment, in order to maximize the sensitivity by making high intensity low energy narrow band beam tuned at oscillation maximum, off-axis (OA) scheme is adopted for the first time[23].

Recent results from the SK [5], K2K [8] and MINOS [20] experiments point at $\Delta m^2_{23} = 2 \sim 3 \times 10^{-3}$ eV^2. At this parameter, the oscillation maximum is at around the neutrino energy of $500 \sim 700$ MeV at the SK; i.e., 295 km away from the source. In addition, the high energy neutrinos ($\gtrsim$1 GeV) do not only contribute to the measurement of the oscillation but become background sources for low energy neutrinos via the neutral current interaction or the inelastic scattering. As these physics condition prefers the high intensity narrow band low energy neutrino beam, we use the OA scheme as a solutions to meet the requirement.

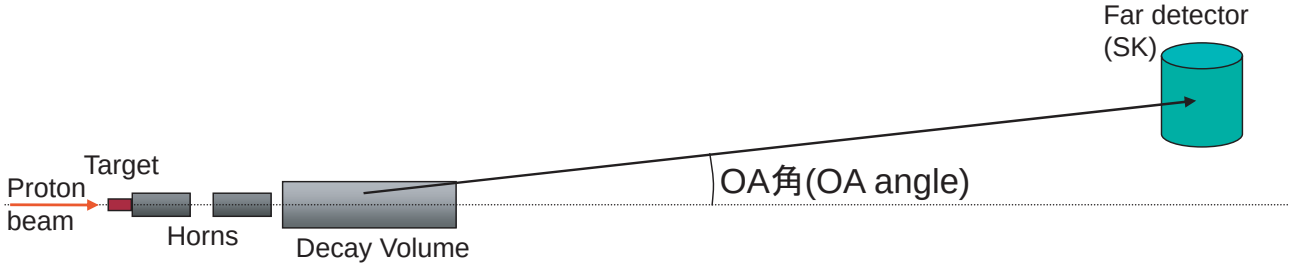

Figure 2.1: Schematic of the Off-axis beam

In on-axis beam, the neutrino detector is placed on the same axis as the one to which proton beam, the target, the electromagnetic horn and the decay volume are aligned. In this case we get broad neutrino energy spectrum (the Wide Band Beam:WBB) as is used in the K2K experiment. The detector is placed at a few degree (OA angle) off from the beam axis in the OA beam as shown in Fig. 2.1. The kinematics of pion decay for the on-axis and the OA beam is illustrated in Fig. 2.2. The neutrino energy is proportional to the energy of the parent π meson when the OA angle is 0 (WBB),

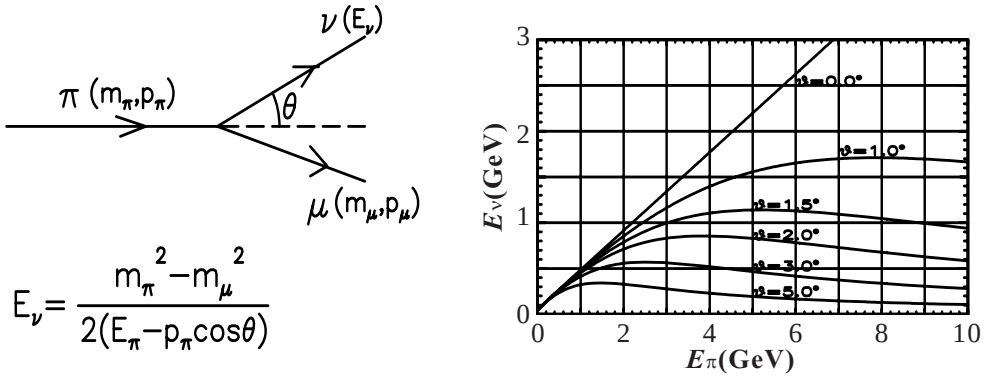

Figure 2.2: Kinematics of the Off-axis beam

while it is almost independent of the π meson energy with non-zero OA angle. Since pions in a wide momentum range contribute to narrow energy range of neutrino, a narrow intense neutrino beam is obtained.

2.1.2 Expected beam

Expected neutrino properties are estimated with the MC simulation in which the geometry of neutrino production equipments are coded. The expected number of total and CC interactions in 22.5 kton fiducial volume of SK is 2,300events/yr and 1,700events/yr, respectively, at 2.5degree off-axis in the case of no oscillation with 30 GeV, 0.75 MW, 3000 hr/yr operation. Expected energy spectra at SK are plotted in Fig. 2.3. Peaks of the energy spectra are at 780 MeV and 600 MeV for 2 and 2.5 degree off-axis, respectively. Contamination of ν_e in the ν_μ beam is $\sim 0.4\%$ at the peak energy of ν_μ spectrum.

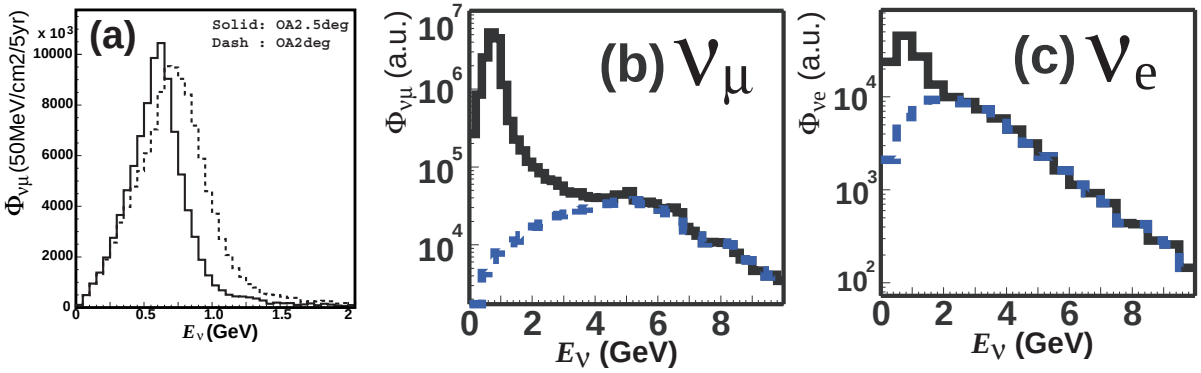

Figure 2.3: Expected neutrino spectra. (a)Energy spectra of ν_μ fluxes for different off-axis angle with 30 GeV, 0.75 MW, 3,000 hr/yr operation. (b) ν_μ flux. Solid is total and dashed line is contribution from Kaon decay. (c) ν_e flux. Solid and dashed lines are total and contribution from Kaon, respectively.

2.1.3 Overview

The layout of neutrino facility in J-PARC is illustrated in 2.4. The neutrino beam line consists of:

- Primary proton beam line,
- Target station,
- Decay volume/pipe,

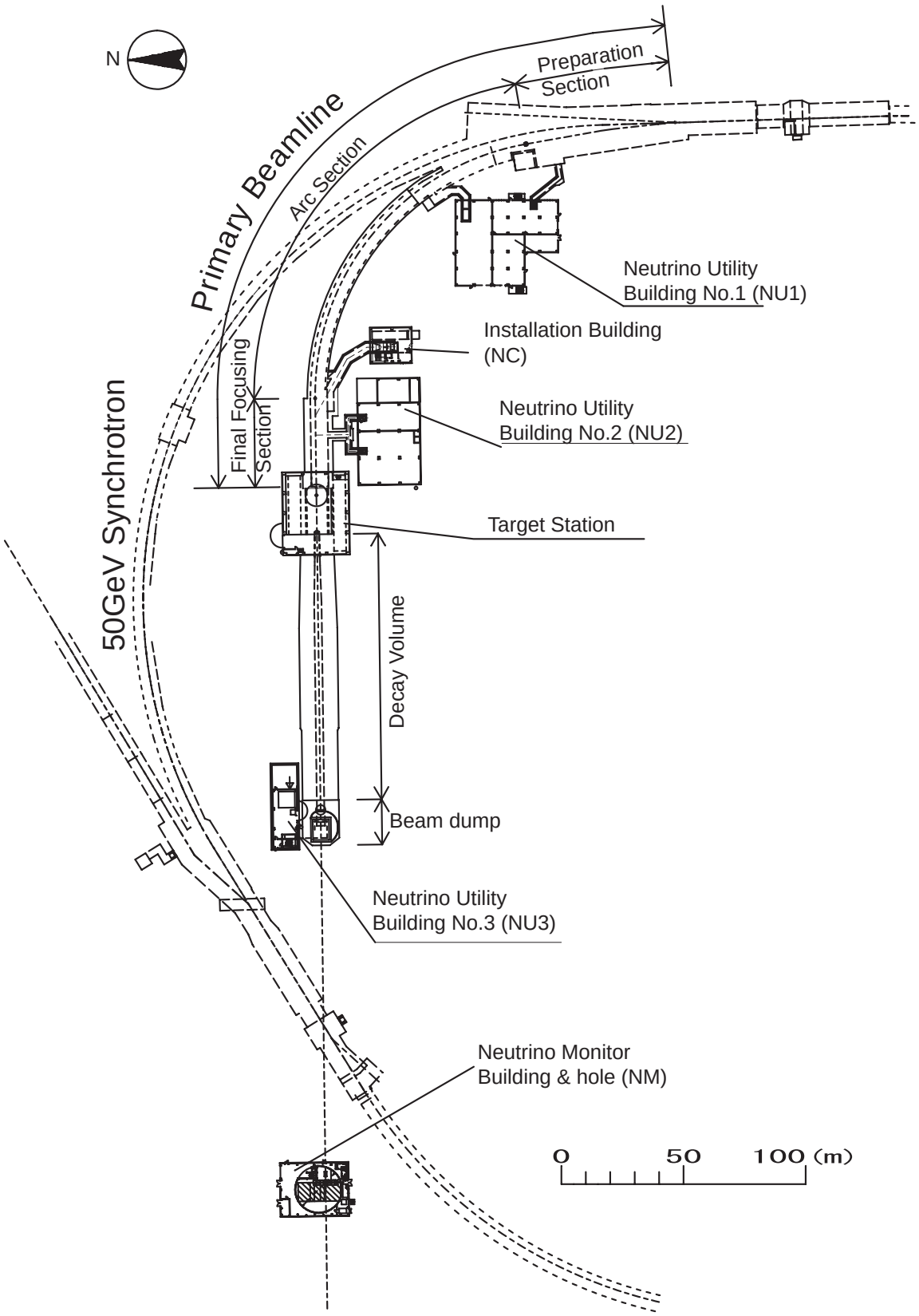

Figure 2.4: The layout of neutrino facility complex

- Beam dump,
- Muon monitor,
- Near neutrino detector,

and several utility buildings.

Special features of T2K beam line are (1) the first use of superconducting (SC) combined function magnets in the primary proton beam line, and (2) the first application of OA beam [23]. The use of the combined function magnets enabled to reduce cost while keeping large acceptance of the beam line. The OA beam can produce low energy high intensity ν_μ beam with adjustable sharp peak in the energy spectrum. The position of the peak will be tuned at energy of oscillation maximum to maximize the sensitivity. In order to have tunability of the neutrino energy spectrum, the neutrino beam line is designed to cover OA angle from 2 to 2.5 degree.

Proton beam is extracted from 50-GeV PS in single turn (fast extraction). The design intensity of the beam is 3.3×10^{14} protons/pulse, and repetition period is 3.5 s, resulting in the beam power of 0.75 MW at 50-GeV operation. The "50-GeV" PS will be operated at 30 or 40 GeV in early stage. One pulse (spill) consists of 8 bunches each with 58-ns full width and separated 598 ns, and the total spill width is $\sim$4.2 μs. Possibility to operate with 15 bunches with doubled harmonic number is also being studied.

The primary proton beam line is to transfer a proton beam from the 50GeV-PS to the neutrino production target. It consists of the preparation, the arc, and the final focusing section (Fig. 2.5). The preparation section is the most upstream part of about 54 m long which consists of 12 normal

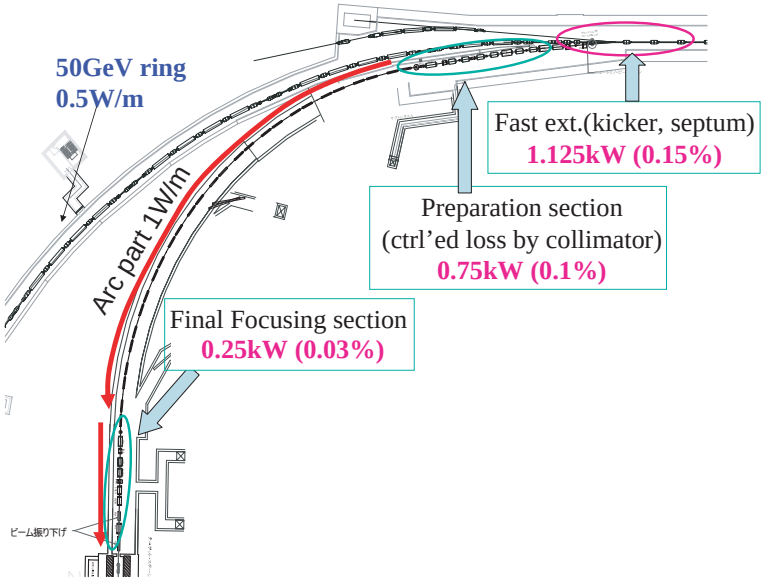

Figure 2.5: Assumed beam loss in the primary proton beam line.

conducting magnets and collimators. Clean beam matched with the following arc section is prepared by the magnets and the collimators. It is designed to accommodate the beam emittance of 60π mm·mrad. In the arc section, the proton beam is bent about 80° toward the Kamioka direction by 28 superconducting combined function magnets. The dipole and quadrupole components of the magnets are 2.586T and 18.62T/m for 50GeV operation. Radius of the arc section is 104.4m and the length is about 150 m. The final focus section is the downstream of the arc section and consists of 10 normal conducting magnet. The beam from the arc section is shaped to be suitable for the neutrino target. Intensity, position, profile and loss monitors are installed along the primary beam line to monitor/keep good beam conditions during the experiment. Beam loss of 750 W, 1 W/m and 250 W are assumed in the preparation, arc and final focusing section, respectively (Fig. 2.5). Thickness of radiation shielding is determined based on the assumption.

Target station accommodates a production target and electromagnetic horns. The target is a $\sim$3-cm diameter and 90-cm long Graphite rod (corresponding to 2 interaction length). About 80% of incoming protons interact with the target material. Heat load from the beam is about 60 kJ/spill ($\sim$20 kW). The target is cooled by forced-flow Helium gas in order to remove the heat. The target is followed by three electromagnetic horns which focus generated pions to forward direction. They are driven by pulsed current of 320 kA at peak synchronized with the proton beam timing. The first horn and the target is protected from accidental hit of miss-steered proton beam by a kind of collimator called baffle which is placed just upstream of the target & 1st horn. In order to reduce Tritium and NOx production, the target station is filled with Helium gas. In order to separate the 1atm Helium gas and primary line vacuum, beam window is placed at the upstream entrance of the target station. It is made of Ti alloy and is cooled by Helium gas. Everything inside the target station will be highly radio-activated and will never be accessible by hands once beam operation starts. All the beam line components will have to be maintained remotely.

The decay volume (DV) is a free space down stream of the horn where pions decay in flight into ν_μs and muons. The length between the target and the end of the decay volume is about 110 m. DV is filled with helium gas to reduce pion absorption, and is surrounded by concrete shield of about 6 m thick. The wall of Helium vessel is water cooled to remove heat load by the beam.

The beam dump is placed at the end of DV and stops hadrons such as remaining protons and secondary mesons. The dump consists of graphite blocks of 3.15 m thickness, 0.9-m thick Copper and 1.5-m thick Iron from upstream to downstream. The graphite blocks are cooled by Aluminum block in which cooling water pipes are embedded.

The Muon monitor is placed just behind the beam dump, where is called muon pit, to detect muons. While almost all hadrons are absorbed by the beam dump, muons of energy > 5 GeV can penetrate the beam dump. Expected muon flux in the muon pit is $\sim 10^8$/cm^2/spill. The muon monitor is designed to provide pulse by pulse information on the intensity and profile (direction) of the beam.

At 280 m from the production target, neutrino detectors will be placed in order to measure neutrino beam properties. Detail of the near detector is described in the detector section.

2.1.4 Overall status and schedule

The neutrino beam line facility was approved by the Japanese government in Dec. 2003 and the construction was started in April 2004 and will complete in March 2009.

In FY2004-2005, civil construction of 50-m part of the decay volume has been finished. In FY2005-2006, the construction of primary beam line tunnel is in progress. In FY2006, the construction of the target station will start. All the remaining tunnels and buildings will be constructed in the last two years, FY2007-2008. R&D and design, production of beam line components are in progress as described in the following sections. Installation of primary line components will start in FY2007 and all the secondary beam line components will be installed in FY2008.

2.2 Normal conducting magnet

Based on the beam optics requirements, parameters of the magnets such as magnetic field strength and gap heights were determined as shown in Table 2.1.

Engineering design of the magnets in the preparation section has been done. Fabrication is in progress, and will be completed by the end of FY2006. After magnetic field measurement, installation of the magnets will be carried out in summer 2007

For the final-focus magnets, engineering design is in progress. Fabrication will be done in FY2007, followed by magnetic field measurement and installation to the final-focus section in 2008.

Commissioning of the magnets will be done in end of 2008 for both preparation and final-focus magnets.

Table 2.1: Parameters of the normal-conducting magnets.

Name	Type code	Optical Gap[mm]		Magnetic Field	Length [mm]	Magnet Gap [mm]		Outward form [mm]		
		Gap	width	[T]		Height	width	W	H	L
PH1	6C220MIC	48	134	1.000	600	90	300	900	730	980
PH2	6C220MIC	63	176	1.000	600	90	300	900	730	980
PQ1	Q460MIC	200 (pole diameter)		0.910	3,000	200		1,350	1,350	3,410
PQ2	Q360MIC	150 (pole diameter)		0.840	3,000	150		1,030	1,030	3,340
PD1	8D360	134	150	1.898	3,000	160	400	1,400	724	3,380
PD2	8D260	101	160	1.898	3,000	130	400	1,400	694	3,380
PV1	5D320MIC	128	60	1.000	1,000	150	250	600	1,100	1,400
PQ3	Q330	150 (pole diameter)		0.910	2,000	150		1,280	1,280	2,350
PV2	6D220	98	113	1.000	1,000	120	300	620	1,400	1,290
PQ4	Q360	150 (pole diameter)		0.863	3,000	150		940	940	3,370
PH3	7D220	48	134	1.000	1,000	120	300	1,200	600	1,400
PQ5	Q240	100 (pole diameter)		0.780	2,000	100		726	726	2,500
FQ1	Q240	100 (pole diameter)		0.648	2,000	100		726	726	2,500
FV1	4D220	51	82	1.000	1,000	120	200	1,400	620	1,290
FH1	4D220	83	72	1.000	1,000	120	200	1,400	620	1,290
FH2	10D414	141	91	1.000	750	200	500	1,220	2,240	1,400
FQ2	Q350	150 (pole diameter)		0.785	2,500	150		940	940	2,870
FQ3	Q350	150 (pole diameter)		0.800	2,500	150		940	940	2,870
FH2	10D414	163	90	1.000	750	200	500	2,240	1,220	1,400
VD1	8D340	92	167	1.730	2,000	130	400	694	1,400	2,380
FQ4	Q330	150 (pole diameter)		0.594	1,500	150		1,200	1,200	3,000
VD2	8D360	90	185	1.740	3,000	130	400	694	1,400	3,380

The normal conducting magnets will be placed in very high radiation environment, and hence be strongly radio-active. It is necessary to minimize working time on maintenance or replacement of the magnets. Various components which enable shortening the work time such as quick connection/disconnection system for water pipe and current lead, as well as remote sling tools to avoid close approach to the magnets, have been developed.

2.3 Superconducting combined magnet system

As stated previously, the arc section consists of 28 superconducting combined function magnets. The section also contains 3 corrector coil packages, which is the combination of normal and skew dipole magnets. The cross section of the magnet is shown in Fig. 2.6 and the main parameters are summarized in Table 2.2.

Table 2.2: Main Parameters of Superconducting Combined Function Magnet

Item	Value	Value
Beam Energy	50 GeV	40 GeV
Dipole Field	2.586 T	2.070 T
Quadrupole Field	18.62 T/m	14.90 T/m
Magnetic Length	3.3 m	3.3 m
Operation Current	7345 A	5876 A
Operating Temperature	< 5 K	-
Load Line Ratio	75 %	60 %
Inductance	14 mH	-
Stored Energy	386 kJ	247 kJ
Magnet Coil Inner Diameter	173.4 mm	-
Beam Tube Inner Diameter	154.1 mm	-
Magnet Yoke Outer Diameter	550.0 mm	-
Magnet Shell Outer Diameter	570.0 mm	-

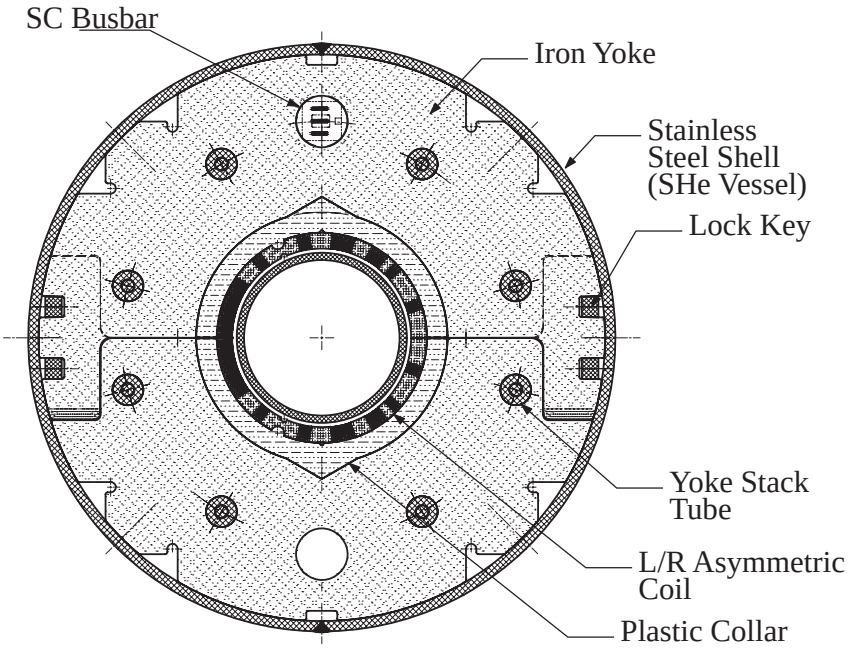

Figure 2.6: Cross Section of Superconducting Combined Function Magnet

The 41 turn left-right asymmetric coil consists of 2 blocks on the high field side and 5 blocks on the low field side. A pair of top and bottom coils, which are mirror symmetry, produce a dipole field of 2.586 T, and a quadrupole field of 18.62 T/m with an operation current of 7345 A for 50 GeV operation with sufficiently good field quality. The coils are wound from the conductor used for the CERN-LHC arc dipole magnet outer layer coil. The plastic collars are made from glass-fiber filled phenolic plastic, which is equivalent to that used for the RHIC magnets. The collars work as ground insulation, which simplifies the assembly process. The RHIC type yoke structure fixes the coil size with the compression pre-stress of 80 MPa providing a mechanical stability as well as good field quality. Construction of the magnet is completed with a 10 mm thick stainless steel shell, which also serves as the helium vessel.

The magnets are connected in series and powered by a single power supply. Each of the magnets is protected by a cold diode and quench protection heaters. The cold diodes are those used for LHC arc quadrupole magnets. The quench detection system, which triggers the quench protection heaters, is based on the system developed by CEN Saclay (France) and will be supplied by Saclay.

The cryostat design is based on that of the LHC arc dipole magnets. The cryostat encases the two magnets in series constructing a doublet. Each of the magnets is mechanically supported by two support posts, and they are connected by bellows to decouple mechanically. The LHC common parts are either acquired directly from CERN or purchased from the company who produces the LHC parts with technical supports from CERN.

The corrector package consists of normal and skew dipole coils that are wound using the BNL (USA) developed direct winding technology. Each coil produces 0.1 Tm integral dipole field at the operation current of about 50 A. The package is developed and is expected to be supplied by BNL.

The development of the combined function magnets is started in 2002. Two full scale prototype magnets were built in JFY 2004. The bidding of the production magnets and cryostated doublets was won by Mitsubishi Electric, and two production magnets were built in JFY 2005. Assembly performed at Mitsubishi Electric is shown in Fig. 2.7. All the magnets are tested in vertical cryostat, and excited up to 7700 A (105 % of 50 GeV operation current) without any spontaneous quenches. The quench protection scheme was also tested and was proven to be safe with a sufficient margin. The

field qualities were measured at a warm test bench as well as the vertical cryostat. The field qualities of the magnets are reproducible and meet the optics requirements. The first cryostated doublet which contains two prototype magnets were also completed and waited for testing.

Figure 2.7: Superconducting combined function magnet assembly at Mitsubishi Electric.

The construction schedule of the arc superconducting magnet system is as follows. In JFY 2006, twelve combined function magnets and six cryostated doublets will be built. The design of the corrector package as well as the quench detection system will be fixed in early JFY 2006 and fabrication will be started within this fiscal year. The specification of the power supply and the transfer line, which connects ground level refrigerator and underground magnet system, will be defined also. In JFY 2007, fourteen (or twelve) magnets and seven (or six) doublets will be built. The installation of the doublet may start in the end of JFY 2007. The fabrication of the corrector packages will be completed in summer 2007 and will be installed in the system within this fiscal year. The fabrication of the quench detector will be completed in March 2008. The power supply will be purchased in JFY 2007. The fabrication of the transfer line will be started in JFY 2007. In the JFY 2008, the rest of the fabrication of the system as well as the installation will be finished until December. The system commissioning without beam will be started in January 2009 and ended in March. The system will be ready for beam in the beginning of JFY 2009.

2.4 Primary Proton Beam Monitors

In the T2K experiment, four types of beam monitors will be installed to measure the primary proton beam properties; 1) Beam Intensity Monitor, 2) Beam Position Monitor, 3) Beam Profile Monitor, and 4) Beam Loss Monitor.

2.4.1 Beam Intensity Monitor

A current transformer (CT), which is made of a toroidal magnetic core and a coil wound around the core, is employed to measure the proton beam intensity since it is non-destructive, simple and established technology. Finemet(FT-3M), produced by Hitachi Metal Co., is chosen as the core material

since it has higher saturation flux density than usual core material such as Permalloy or ferrite. Four CTs will be installed; at the beginning and at the end of the two normal-conducting sections.

Two prototype CTs were manufactured and tested. The first prototype with an inner diameter of 190mm was installed in the K2K proton beam line to check the basic performance of the intensity monitor. The beam intensity measured with this CT agreed with the intensity measured with K2K's CT with a relative deviation of about 0.8% upto the K2K beam intensity of $\sim 6 \times 10^{12}$ppp.

The second prototype was made to prove the performance. The inner diameter was expanded to 260mm to fit the real beam pipe size including the flange part. By performing a high current test and a temperature dependence test, it was confirmed that the output signal is linear to the input pulse charge within 1.3% upto corresponding charge to one bunch of J-PARC full-intensity beam, and no significant temperature dependence was found.

The engineering design is being finalized by the end of 2006. Fabrication will be done in FY 2007, and the installation will take place in FY 2007 (in the preparation section) and in FY 2008 (in the final-focus section).

2.4.2 Beam Position Monitor

The beam center position is required to be measured within 0.5 mm accuracy. Beam position monitors should be operational under the highest beam intensity. The electro-static monitor (ESM) with four pick-up electrodes surrounding the beam-axis is employed. Beam position is obtained from the left-right (or up-down) asymmetry of the signal amplitudes. This monitor is non-destructive and the structure is simple. We install 20 beam position monitors distributed along the beam line.

A prototype was constructed and exposed to the K2K primary proton beam to check the basic performance(Fig. 2.8). Position resolution is demonstrated to be better than 0.3 mm which satisfy the

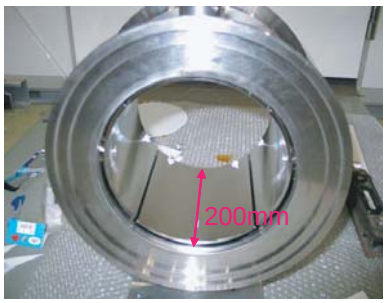

Figure 2.8: ESM prototype.

requirement of 0.5 mm.

Engineering design for production is being finalized. Mass production will start within FY2006. The installation is to be completed by the fall 2008.

2.4.3 Beam Profile Monitor

Beam profile monitors are required to measure beam center position with 0.5 mm precision and profile width with 0.35 mm and 0.7 mm precision for the most downstream and the other locations, respectively. These requirements are to control the neutrino beam direction within 1 mrad and to protect the target from breakdown.

A Segmented Secondary-Emission Monitor (SSEM) will be used as a profile monitor. The monitor consists of a HV anode foil and two cathode layers of segmented foils (x and y) in both sides of the anode foil. Secondary electrons are emitted from the cathode foils when the proton beam passes through the cathode material, giving a positive signal read out from the cathode foils. In order to reduce beam loss caused by interactions of protons in the foils, very thin Titanium foils of 5 μm thick,

which corresponds to 1.8×10^{-5} interaction length, are used for both anode and cathode layers. In order to minimize the beam loss and the deterioration of the foils, the monitors are retracted away from the beam line when not in use. They are equipped with a driving mechanism which is operational under environment of high-radiation, vacuum, and cryogenic temperature. We will install 17 SSEMs (each with x & y) along the primary beam line.

Several prototypes have been made and series of test measurements have been performed using K2K primary proton beam and KEK-NML beam line. Fig. 2.9 shows the measured beam profiles in the test. The outcome of the prototyping and the measurements are summarized below;

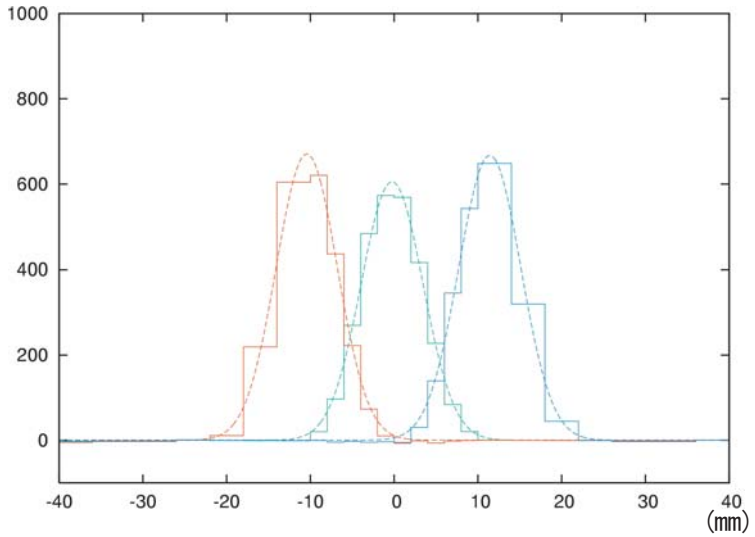

Figure 2.9: Measured beam profiles for three beam positions.

- Secondary emission efficiencies of several materials (Al, W, Ti, Cu-Be, Cu) were measured. It is found that Titanium has comparable efficiency with the other candidate materials.
- Position resolution is found to be better than 0.25 mm. (Requirement: 0.5 mm)
- Beam width can be measured with precision of 0.23 mm (Requirement: 0.35 mm).
- Life of Ti foil (when the secondary emission efficiency becomes 1/e) is measured to be 2.7M pulses (27k pulses) at 1/100 (full) intensity operation, which are good enough numbers for our usage.
- Signal and grounding cable configuration has been optimized to minimize noise.
- The method to fix this very thin foils is established.

In conclusion, we can go ahead with SSEM since it is demonstrated that the basic mechanical design works and it satisfy all our requirements on the performance.

Engineering design is now in progress. Some of the SSEMs will be used in cryogenic environment. Operation test of some components, such as moving mechanism, limit switch, in low temperature and vacuum environment is now underway. In order to test radiation hardness of the components, irradiation test is planned within several month. Within FY2006, detailed specifications will be fixed and mass production will start. Two production model will be fabricated in FY2006, and 15 SSEMs will be fabricated in FY2007. The installation is to be completed by the fall 2008.

2.4.4 Beam Loss Monitor

To monitor the beam losses, Beam Loss Monitors (BLMs) will be distributed along the beam line. If BLMs detect large beam loss, accelerator operation will be vetoed to minimize the damage to beam-line components and environmental radiation level. In the arc section, the maximum beam energy loss is required to be less than 1 W/m. Therefore, the BLMs are required to continuously monitor the beam loss throughout this section. Considering the signal dynamic range, costs, and radiation hardness features, ionization chamber is a good candidate for the BLM. Additionally, air-filled ionization chambers don't require a gas circulating system.

To check the basic operation of the BLM, two prototype monitors were made and tested at the K2K beam line. The measured charge was consistent with the expected values from the MARS simulation.

The design of a readout circuit system and integration to the interlock system should be worked out. The installation should be completed by the end of FY 2007 for the preparation section, and by fall 2008 for the final-focus section.

2.4.5 Optical Transition Radiation Detector

An optical transition radiation detector (OTR) will be used to measure beam position and profile just upstream of the target [26]. Thin Ti-alloy foil will be placed in front of the target. The OTR light from the foil is lead to imaging detector made of MCP-CCD chain through series of mirrors. It is confirmed with MC simulation that the basic concept works in principle. Currently conceptual design is being done. The OTR system is the one of contributions expected from Canada.

2.5 Vacuum System

Requirements on the vacuum level of the primary-proton beam-line are as follows:

- $\ll$ 1Pa everywhere to keep the beam loss due to the residual gas negligibly small,
- $\sim 10^{-6}$Pa at the boundary to the main ring.
- $\ll 10^{-2}$Pa at the boundary to the arc to keep heat flow into the arc less than a few W,
- $\ll 10^{-2}$Pa at the monitor locations to operate beam profile monitors.

To fulfill the requirements, ion pumps are distributed for evacuation at the normal operation stage, while initial pumping will be done with detachable turbo-molecular pumps and their follow-up pumps. Locations of the vacuum pumps are shown in Fig. 2.10.

At the downstream-end of the final-focus section (FF), there is a thin titanium window to separate the beam line vacuum from the target-station helium vessel. Fast-closing valves will be installed at the end of the FF, as well as at the boundary to the main ring, to protect the beam window and main ring vacuum, respectively, in the case of vacuum break.

GEANT simulation was carried out to examine which material can stand for the direct hit of the beam. Deform and stress caused by atmospheric pressure were also calculated by a finite-element analysis.

Stainless-steel was ruled out because it suffers too much thermal-shock stress. Titanium and some aluminum alloy are shown to survive the beam-hit. For the most-upstream part, therefore, 3mm-thick titanium will be used to achieve the high vacuum and low residual radio-activity, while 5mm-thick aluminum alloy will be used otherwise.

Residual radiation level around the upstream magnets should be too high for hands-on operation of flanges. Therefore vacuum flanges with "semi-remote" clamps will be adopted to enable manual disconnection/connection from distant location.

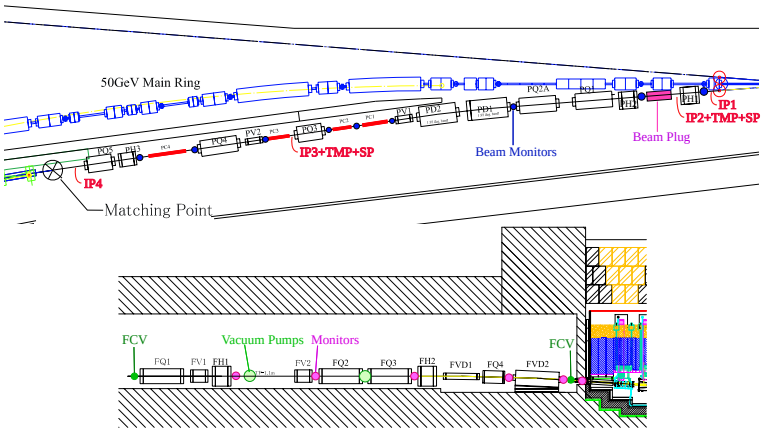

Figure 2.10: Location of the vacuum pumps at the preparation section (upper) and at the FF (lower).

One side of the pair of flanges must move backward after the clamp is un-tightened in order to make space for removal of the equipment. This must also be done manually from some distant location. Development has been almost completed for main-ring vacuum system, and the same mover will be used for the neutrino beam line.

Vacuum equipments should also be radiation-resistant. Present availability is summarized in table 2.3. At present we have no fast-closing valves which can stand for $\sim$1MGy. The only solution seems to place it apart from the beam line by extending actuator rod, and simply replace it every 3$\sim$4 years.

gauges	No organic material.
pumps	1MGy products exist (cables inside limit)
gate valves	100MGy-products exist.
fast-closing valve (valve)	100MGy-products exist.
fast-closing valve (actuator)	100kGy-products only.
cables and connectors	10MGy products exist.

Table 2.3: Commercially-available radiation-resistant products.

Schedule of the vacuum system construction is as follows.

- By the end of JFY2006, fabrication of the beam ducts and purchase of pumps/valves for the preparation section will be done.
- In the summer 2007, installation for the preparation section will be carried out.
  Also in 2007, fabrication and purchase for FF will be done.
- Finally in summer 2008, installation for the FF will be completed.

2.6 Target

We plan to use a graphite bar as a hadron production target since high-Z materials will be melted within a few spills because of high beam intensity. Figure 2.11 shows the conceptual drawing of target system. Because the target has to be placed in the inner conductor of the first horn, the cooling module should be compact. The cooling module consists of a co-axial double layer cooling pipe so that the target and cooling modules can be maintained independent of the first horn. The inner and outer cooling pipes are made of graphite and titanium alloy (Ti-6Al-4V), respectively, because aluminum cannot withstand against the miss-steered beam hit. The target should be completely enclosed by titanium alloy to avoid the oxidization of graphite. Therefore, there are two beam window which

made of titanium-alloy at the both end of the target. The outer surface of the outer cooling tube is coated with plasma-splayed alumina ceramics for the insulation with the first horn.

The size of the target is 3 cm in diameter and 90 cm in length (corresponding to 2 interaction length). 80% of incoming protons interact with the target material. The material for the target is an isotropic graphite IG-43 by Toyo Tanso Co. Ltd., which has a tensile strength of 37.2 MPa. The maximum energy deposit due to a proton beam hit is 190 J/g/spill which corresponds to the expected thermal stress of 7.4 MPa. The IG-43 graphite has an enough safety factor of 3.5, where a material fatigue factor of 0.7 is considered.

The total energy deposit by the proton beam and secondary particles in the target was estimated to be $\sim$60 kJ/spill and the maximum temperature rise reaches 200 K/spill. The required cooling capability for the target is 20 kW. We will use the forced convection of helium gas to reduce the radiation damage of the target by controlling the temperature between about 400 $^{\circ}\mathrm{C}$ and 800 $^{\circ}\mathrm{C}$ where the radiation damage of the graphite is minimum. Helium cooling also has the advantage of reducing radioactive waste water compared to a water cooling. The beam windows is cooled by the helium gas simultaneously with the target.

The feasibility of the helium gas cooling is confirmed by the FEM simulation and the test using the 1/20-scale prototype. The required helium flow rate is 660 $\mathrm{Nm^3/h}$ including 20 % margin. The expected pressure drop at the target cooling path and the heat-exchangers are 0.15 MPa. Production of the helium circulation system is completed and it is confirmed that the gas compressor archived the required flow rate with the pressure difference of 0.2 MPa. We plan to perform the full-scale cooling test with it in 2006.

The detailed design of the target and cooling tubes are in progress. The shape of the downstream window is optimized for the smooth helium flow by using the CFD simulation. The mechanical prototypes of the target and the cooling tubes are produced in order to confirm the machining feasibility. (Fig.2.12) The manufacturing of the target, the graphite cooling tube with 2 mm thickness and the titanium cooling tube with 0.3 mm thickness, the welding of titanium-ally, the brazing between graphite and ti-alloy and the ceramic-coting of the titanium alloy is tested.

The design of the upstream window, the fixation method, alignment mechanism and remote maintenance method of the target system will be completed in 2006. We will made the prototype of the whole target system as same as an actual equipment by the end of JFY 2006. We will perform the helium-flow test with the prototype in 2007. The design modification to include the feedback from full-prototype test and the production of the actual equipment will be finished by the end of JFY2007. The installation into the 1st-horn will be done in 2008.

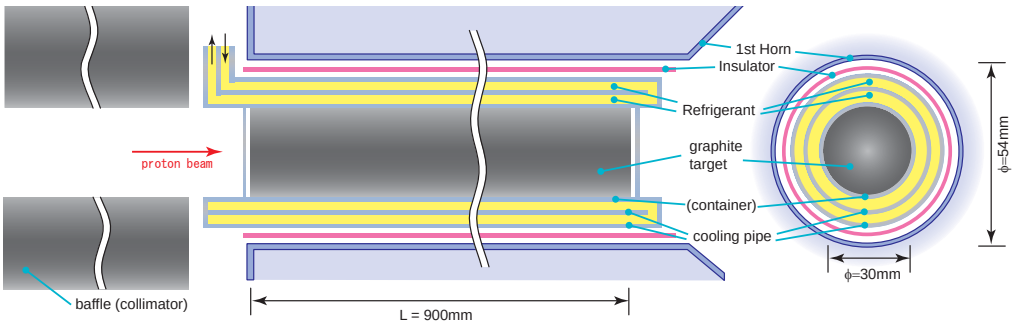

Figure 2.11: Conceptual drawing of the target system of J-PARC ν beam line.

2.7 Horn

An electromagnetic horn system is employed to focus pions generated at the target. Figure 2.13 shows a schematic view of the horn system. It consists of three horns and will be operated with

Figure 2.12: Mechanical prototypes of the target system. The left picture shows the target(bottom) and the graphite inner cooling tube(top). The center and right picture is the titanium outer cooling pipe after the welding with the downstream beam window and after the ceramic-coting, respectively.

320kA peak current generating 2.1 Tesla maximum field. The target is inserted inside the 1st horn inner conductor. The 320kA current causes strong Lorentz force on the conductors. High intensity instantaneous proton beam heats up materials and hence generates thermal shock stress. The horn system will be installed in a helium environment, in which break down voltage is lower than that in atmosphere. Ionization by radiation may father reduce the break down voltage. These issues are carefully studied and detailed design of the horns are being pursued. Figure 2.14 shows a prototype of the 1st horn. It will be tested with 320kA current in this fiscal year (FY2006).

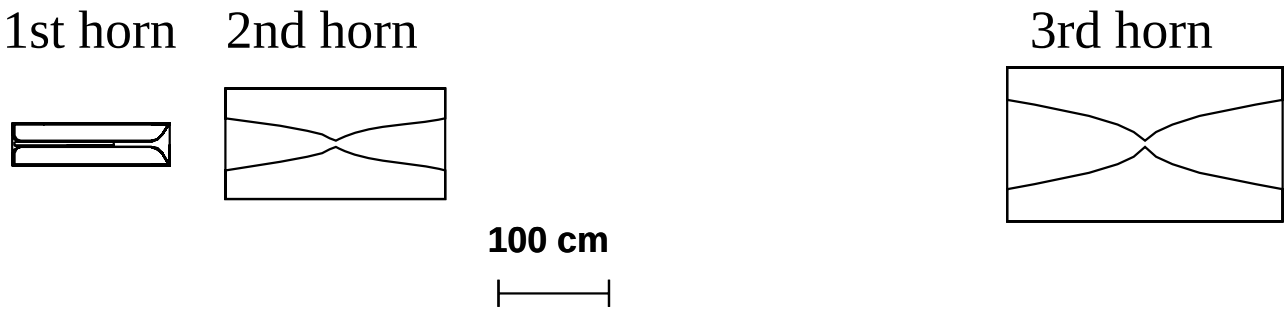

Figure 2.13: Schematic view of the horn system.

Figure 2.14: 1st horn prototype

A horn is hanged from an iron box support module. The support module itself is hanged from the target station service pit. With a $\sim$ 1MW beam, these horns and target will become highly radioactive. Maintenance must be done fully remotely. When one of the horns is broken, the horn and its support module is transported to the target station hot cell by a remotely-controlled crane. Then, the module and horn is decoupled and a new horn is coupled to the module. These decoupling and coupling are done remotely by rotating long shafts which penetrate the support module. R&D of the remote coupling of horn itself, water path and striplines have been done.

The R&D including production of prototypes will continue throughout FY2006. Life-time tests with 320kA current operation for the 1st horn and 3rd horn will continue from FY2006 to FY2007 with those prototypes. The remote maintenance will be checked with the Target station He-chamber mock-up and the prototype of the support module. All real components will be produced in FY2007 and installed in FY2008. Tests of the remote maintenance and current operation with the final setup will be done in FY2008 during/after the installation.

2.8 Target station

The target station is the building and facility where pion production target and pion beam focusing horn magnet locate. Proton beam of 50GeV and 15μA is focused by the final focusing section of the beam-line in front of the target station and hit the target at 12-m deep underground. Pions produced at the target are focused by the three horn magnets along the beam-line and sent into the decay volume which follows the target station. It is essential for the safety to effectively shield the radiation and remove the heat created by the secondary particles such as pions produced by the proton hitting the target. Thus, the keys in the design of the target station are radiation shielding, cooling, and maintenance.

Target station consists of the following five elements; 1) Target, horn and their support structure, 2) Radiation shielding, 3) Surface building, 4) Underground machine room, 5) Storage room of radioactive materials. Figure 2.15 shows the cross section and side view of the target station.

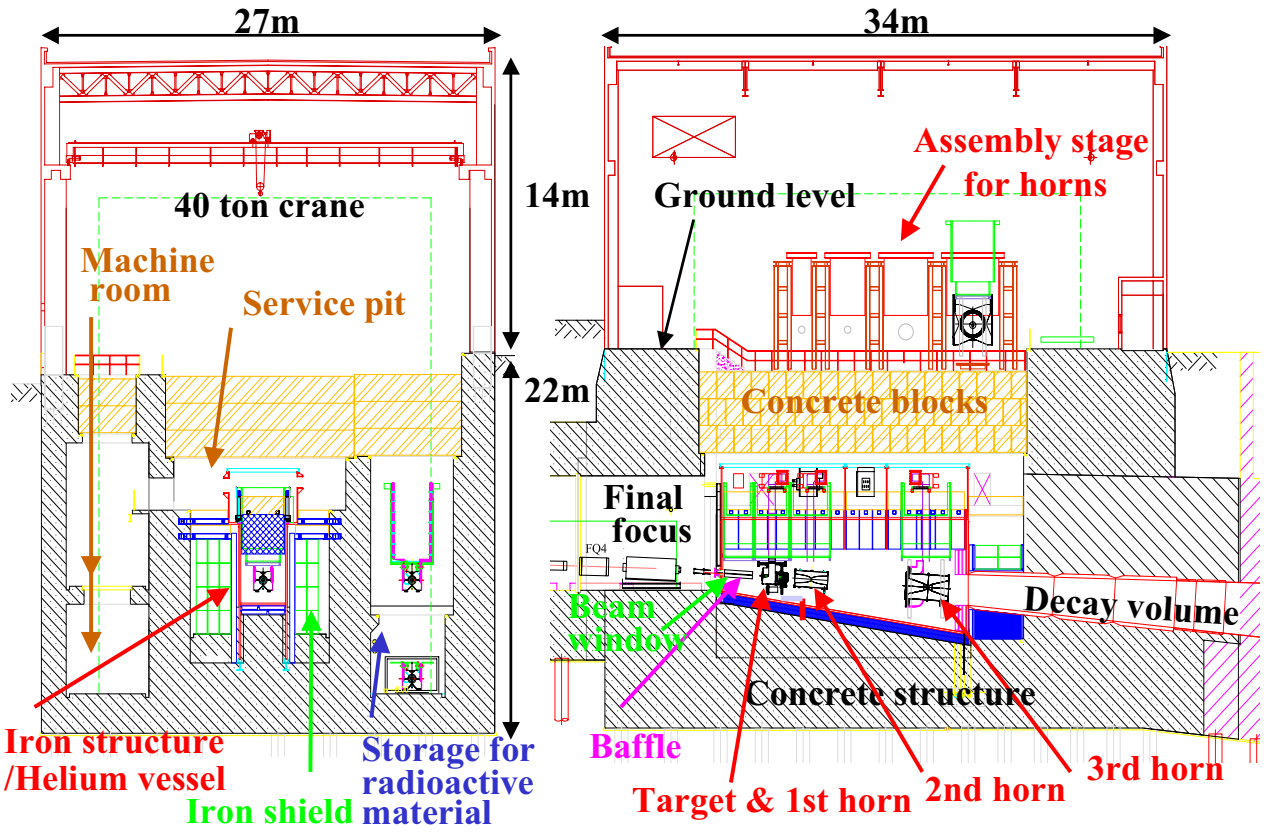

Figure 2.15: The target station

In order to avoid activation of the air, target and the three horns are in an iron container filled with helium gas. The weight of target and horns are supported by an iron support structure from the floor. Surrounding the helium container are the iron shielding blocks which are further surrounded by concrete shielding. Since significant temperature rise is expected in the support iron structure, helium container and the iron shielding blocks, they are cooled at their surfaces. Connect/disconnect

of pluming and power lines is done by human in the empty space of the concrete shielding above the target and horn, which is called service pit. Next to the service pit, there is an underground machine room where various cooling machines are placed. A storage for radioactive materials locates on the other side of the service pit where damaged radioactive horn and target will be temporarily stored. The vacuum of the primary beam final focusing section is separated by a beam window foil at the upstream end of the helium container. The upstream edge of decay volume is connected to the helium container. At the beginning of the decay volume is made of water-cooled iron shielding, called DV collimator, which reduces the heat load in the concrete section of the decay volume.

The status of the target station is as follows:

- The detail design work for the building finished in Mar. 2005, and the contract of the construction is under bidding.
- The detail design work for the cooling apparatus finished in Mar. 2005.
- The detail design work of the support structure and the most upstream part of the decay volume finished in Mar. 2006, and the contract of the assembly is under bidding.
- The basic design work of the upper concrete shields finished in Mar. 2006.
- The inner iron and concrete shields are under designing.
- The DV collimator is under designing.
- The beam window and final monitor chamber are under designing by RAL and TRIUMF, respectively.

Figure 2.16 shows the future schedule of each component of the target station.

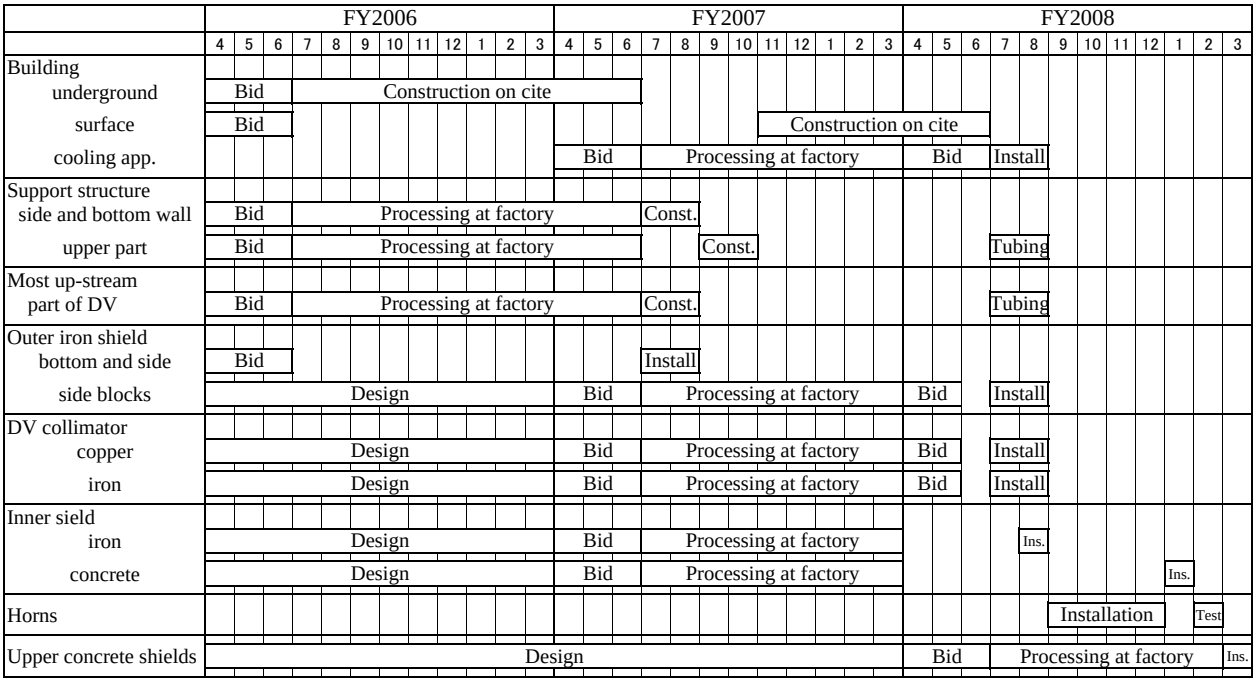

Figure 2.16: The schedule of target station

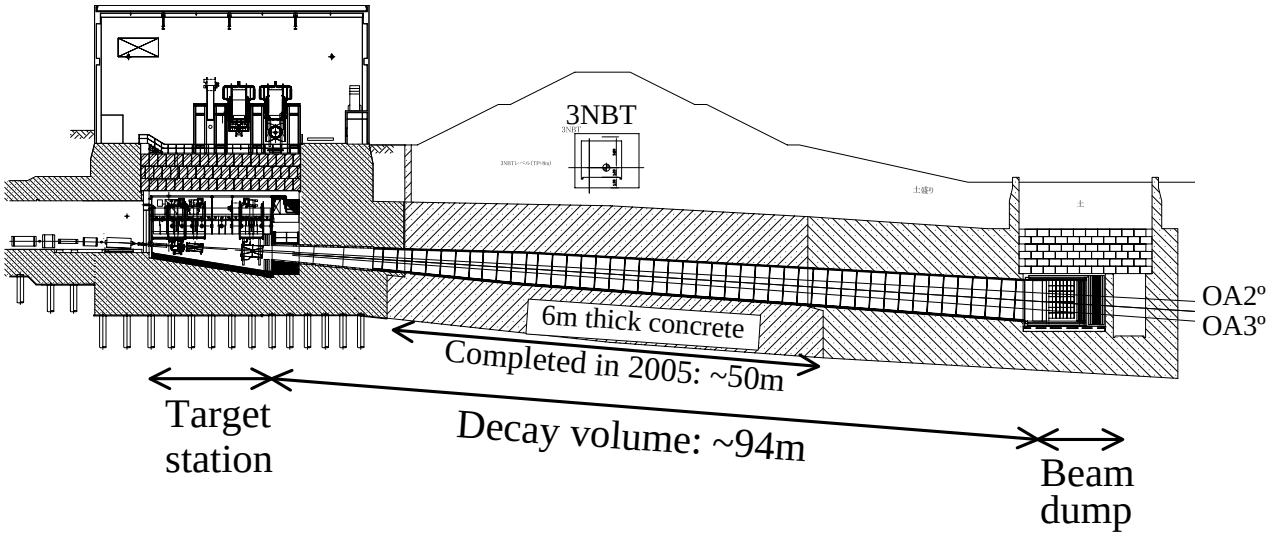

Figure 2.17: The decay volume

2.9 Decay volume

Construction of the upstream 50 meter of the decay volume started in July 2004 and finished in Dec. 2005. Figure 2.17 shows the side view of the decay volume. The four iron plates, on which the cooling circuits called the plate-coil were attached by welding, were welded at the factory to form a rectangular box, and 29 boxes were connected by welding to form the 50 m long tunnel in which pions decay into muons and neutrinos. Figure 2.18 shows the 50 m long iron tunnel before surrounded by concrete wall. After constructing 6 m thick concrete wall surrounding the iron tunnel, the 40 cooling circuits were formed by connecting the plate-coils by U-shape tubes. Figure 2.19 shows the inside of the decay volume. The most upstream part of the decay volume will be assembled by the 20 cm thick iron plates with plate-coils and connected to the helium vessel of the target station in FY2007. For the remaining downstream part of the decay volume, the iron plates have been fabricated with the plate-coils to form the 26 m long iron tunnel. This downstream part of the tunnel will be assembled with the concrete wall in FY2007, and will be connected to the helium vessel of the beam dump in FY2008.

Figure 2.18: The 50 meter iron tunnel

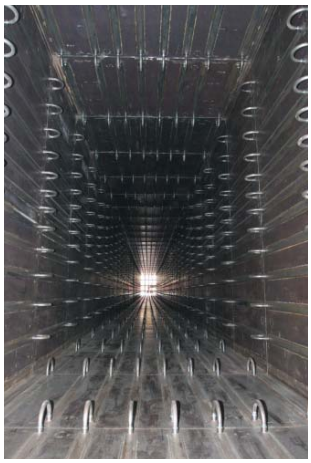

Figure 2.19: The inside of the decay volume

2.10 Beam Dump - Hadron Absorber

The beam dump - hadron absorber, which can deal with a few Mega-Watt of heat, will be installed at the downstream of the decay volume. By the close cooperation with the engineering division of CCLRC Rutherford Appleton Laboratory and with Japanese heavy industrial companies, we have finalized basic design both for the hadron absorber core and for its surrounding helium vessel iron structure in JFY 2005.

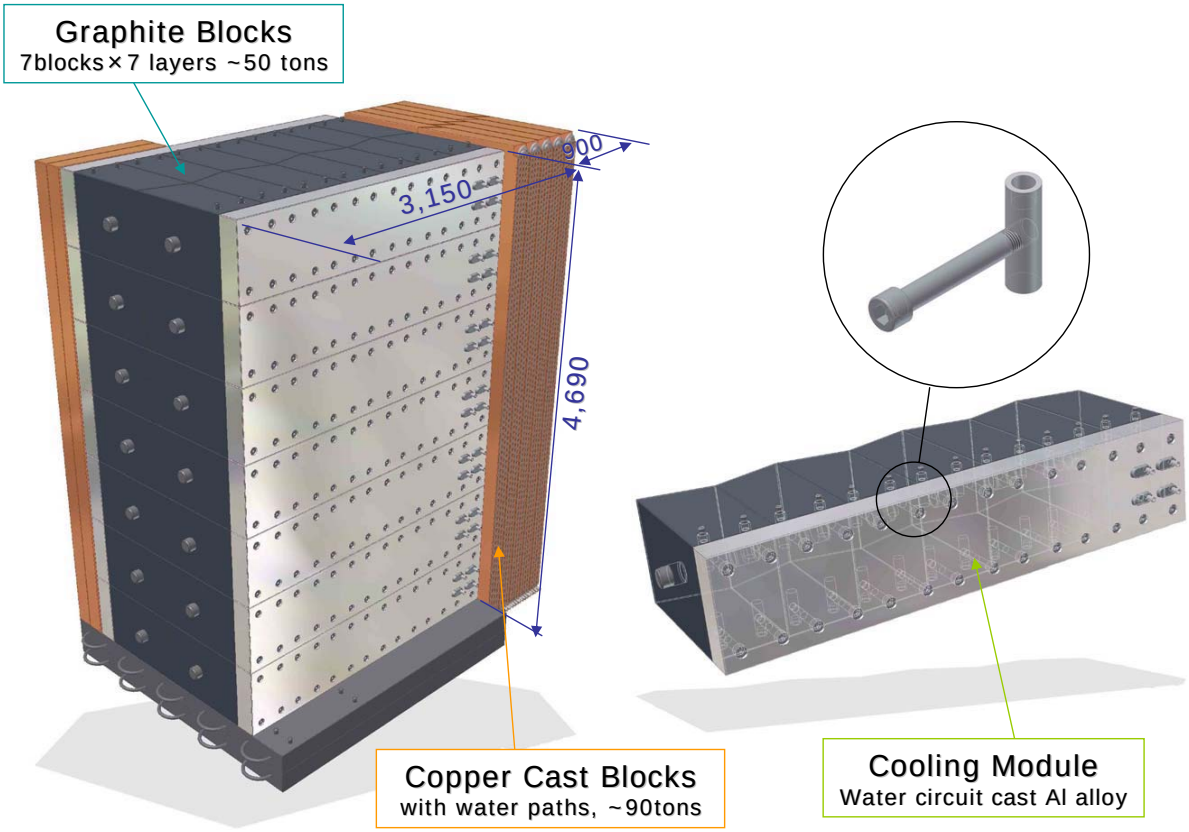

Figure 2.20: The conceptual drawings of the T2K hadron absorber core and its graphite module component

Figure 2.20 shows conceptual drawing of the core. It has a rectangular cross section with about 5 m high and 3 m wide, to handle tunable off-axis beam. The upstream part is composed of large extruded graphite blocks, which has 230 W/m·K heat conductivity, and aluminum-alloy cooling modules with water circuits casted in it. There are 14 units, *i.e.* left/right $\times$ 7 in height. One unit is composed of 7 graphite blocks with cross section of 670mm$\times$450mm and about 1m long, fastened laterally to a cooling module by screws and nut-pins. With help of the scheme we can achieve more than 4 kW/m^2·K of heat transfer between the surface of graphite blocks and the cooling module. The downstream part of the core is composed of 10 (left/right $\times$ 5 layers) large copper cast plates with water paths brazed at one side of the plates.

Figure 2.21 shows typical results of the FEM simulations. In the simulation we assume thermal links between one graphite to another, and also graphite blocks to cooling modules, based on the measurement with a test module. The maximum temperature of the graphite should be lower than 650 degree C, even in the helium environment, to avoid oxidization by the contamination of the atmosphere. Lower primary proton energy, and thus wider beam divergence, is preferred by the tolerance of the graphite core. With 30 GeV primary beam energy, it is turned out that current design can handle beam operation power up to 3MW.

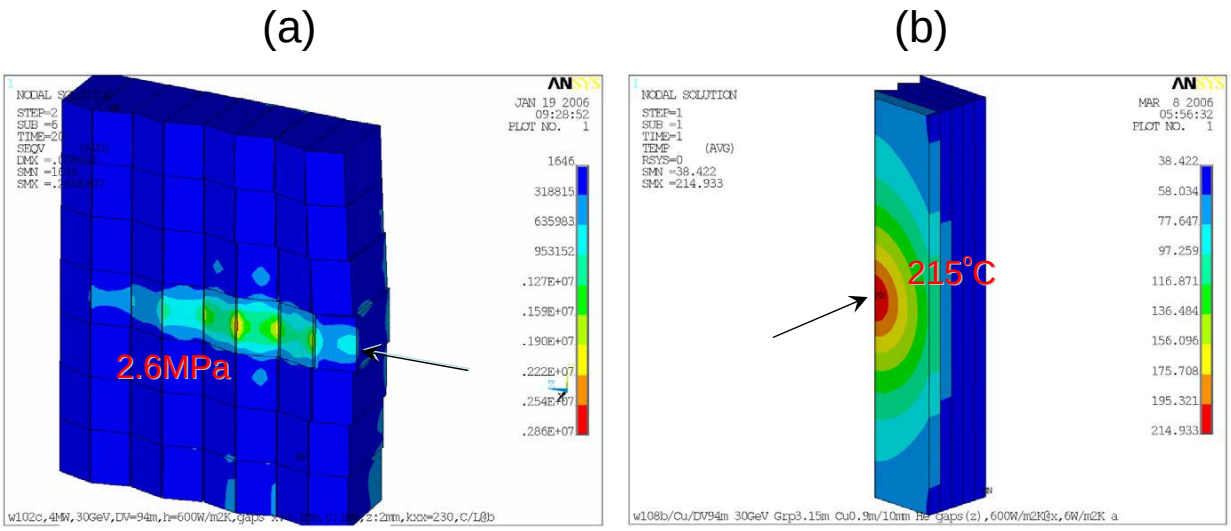

Figure 2.21: The results of the FEM analysis of the core, (a) Von-Mises equivalent stress distribution in the graphite blocks and (b) temperature distribution in the copper plates, for 4MW operation with 30GeV primary proton energy.

In JFY 2006, we will purchase large graphite blocks, and complete detailed designs both for core components and the helium vessel structure. At the same time we will make the first unit of the graphite core module to establish the way of assembly. Whole machining and production will start in JFY 2007, and installation will take place in the end of JFY 2008.

2.11 The muon monitor(MUMON)

Accurate control of the beam direction is essential to reduction of the systematic uncertainty in long baseline experiments. In the case of T2K, 1 mrad change in the neutrino direction corresponds to about 25 MeV shift in the peak neutrino energy, which contributes to the systematic uncertainty in the measurement of Δm^2_{23}. In order to achieve the aimed precision of the experiment ($\delta(\Delta m^2) \simeq 10^{-4}$ eV^2), the direction of the neutrino beam should be controlled and monitored with precision much better than 1 mrad. This is the principle goal of the muon monitor.

The muon monitor measures the direction, profile and intensity of the beam on a spill by spill basis. It will be located downstream of the beam dump and detect high energy (> 5 GeV) muons which penetrate the dump. Because the muons are produced from the same parent particles as the neutrinos, the muon properties are directly associated with those of the neutrinos. The spatial profile and intensity of the muons are sensitive to the condition of the magnetic horn system and the accuracy of the proton targeting. The muon monitor will also provide information necessary for tuning of the beam in the commissioning of the experiment. It therefore needs to be sensitive to the beam condition, e.g. proton beam position at the target.

The expected muon flux at the position of muon monitor is $\sim 10^8$ muons/cm^2/spill at the beam center, which corresponds to $\mathcal{O}(10^{15})$ muons/cm^2 for one year of operation. The detectors must survive this high radiation. Because the muon monitor is the only instrument that can assure the quality of the neutrino beam on a spill by spill basis, a failure of the muon monitor would cause deadtime for the whole experiment. Therefore, the detectors should be robust and stable. Based on the experience in K2K, we chose a combination of a segmented ionization chamber and an array of the semiconductor detectors as the baseline design of the T2K muon monitor.

The ionization chamber is a simple and reliable device to monitor the beam for a long run period. It is also suitable to cover the large area of the beam profile with the large number of devices. Some

weak points are the slow response and the non-strong signal over the unknown backgrounds from the beam dump.

The semiconductor detector has a fast response, and is less sensitive to background because of the large and fast signal. A concern for the semiconductor detector is the long term stability due to the radiation damage. Currently we plan to use the silicon-pad detector for the neutrino beam commissioning (day 1), which can be used for one year. A diamond detector which is an another type of the semiconductor detector with higher radiation tolerance, is also studied as a candidate detector for the T2K MUMON. The diamond detector is extensively studied and developed by RD42 collaboration at CERN [25]. A concern on the diamond detector is the capability of the mass production, which will limit the number of available sensors at day 1. We will use $\sim$20 diamond sensors, among which we have five in our hand now.

We design to construct two detector planes with different sampling intervals: one consisting of the ionization chambers and the other of the semiconductor detectors. Two independent and complementary detectors provide reliable monitor information that is mandatory for the experiment. The MUMON signals will be recorded by the FADC modules commonly used for the T2K beam-line monitor developed at KEK. The MUMON data will be also processed by the beam-line DAQ.

Chapter 3

Near Detector ND280

To achieve the physics goals set out in the introduction, it is essential to have precise measurements of the neutrino beam properties near the target, and measurements of neutrino interaction cross sections and kinematics.

For the ν_μ disappearance study, it is important to measure the flux of muon neutrinos and their spectrum. In addition, cross sections need to be measured for muon neutrino interactions for which the far detector will misinterpret and assign the wrong neutrino energy. For the ν_e appearance study, the flux and spectrum of electron neutrinos must be known, as well as the cross sections for interactions that the far detector will misinterpret as coming from ν_e. To make these measurements to the required precision necessitates a highly segmented large volume detector, capable of charged and neutral particle energy measurements and particle identification.

The reconstruction of the neutrino energy at the near detector is based on Charged-Current Quasi-Elastic (CCQE) interactions, where the neutrino energy E_ν is reconstructed measuring the muon or electron energy E_l and its angle θ_l to the neutrino beam direction as shown by a formula:

$$E_\nu = \frac{m_N E_l - m_l^2/2}{m_N - E_l + p_l cos\theta_l}, \tag{3.1}$$

where m_N and m_l are the masses of the neutron and lepton(=e or μ). The inelastic reactions of high energy neutrinos constitute the background to E_ν measurement with the CCQE. In addition, the inelastic reactions produce π^0's that are the main background for ν_e appearance search. Then the detection of γ's and reconstruction of π^0's is also required.

This chapter describes the detectors proposed to make these measurements.

3.1 Overview of the ND280 Near Detector

The near detector complex (ND280) at 280 m from the target contains a fine-resolution magnetized detector designed to measure the neutrino beam's energy spectrum, flux, flavor content, and interaction cross-sections before the neutrino beam has a chance to oscillate. This detector sits off-axis in the neutrino beam along a line between the average pion decay point in the decay volume and the Super-Kamiokande detector, at a distance of 280 m from the hadron production target.

The ND280 detector consists of the following elements, illustrated in Figure 3.1:

- Magnet: ND280 uses the UA1 magnet operated with a magnetic field of 0.2 T to measure the momenta of penetrating charged particles produced by neutrino interactions in the near detector. The inner dimensions of the magnet are 3.5 m $\times$ 3.6 m $\times$ 7.0 m.

- Pi-Zero Detector (P0D): The P0D detector sits at the upstream end of ND280, and is optimized for measuring the rate of neutral current π^0 production. The P0D consists of tracking planes composed of scintillating bars alternating with lead foil. Inactive layers of passive water in

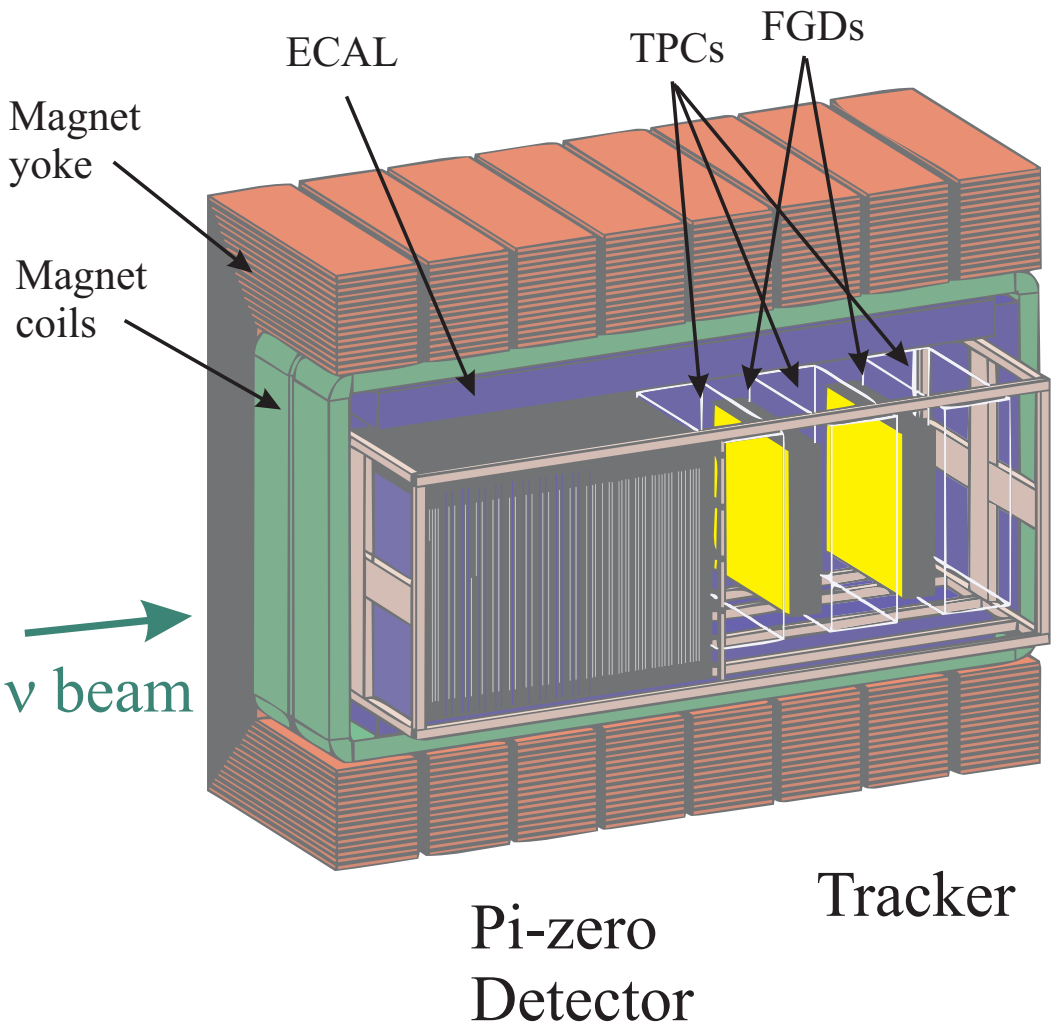

Figure 3.1: Cutaway view of the T2K 280 m near detector. The neutrino beam enters from the left.

sections of the P0D provide a water target for measuring interactions on oxygen. The P0D is approximately cubical, and is covered on all 6 sides by the electromagnetic calorimeter.

- Tracker: Downstream of the P0D is a tracking detector optimized for measuring the momenta of charged particles, particularly muons and pions produced by CC interactions, and for measuring the ν_e background in the beam.

    1. Time Projection Chambers (TPCs): Three time projection chambers will measure the 3-momenta of muons produced by charged current interactions in the detector, and will provide the most accurate measurement of the neutrino energy spectrum. The 3D tracking and dE/dx measurements in the TPC will also determine the sign of charged particles and identify muons, pions, and electrons.
    2. Fine Grained Detectors (FGDs): Two FGD modules, placed after the first and second TPCs, consist of layers of finely segmented scintillating tracker bars. The FGDs provide the target mass for neutrino interactions that will be measured by the TPCs, and also measure the direction and ranges of recoil protons produced by CC interactions in the FGDs, giving clean identification of CC QE and CC non-QE interactions. One FGD module will consist entirely of plastic scintillator, while the second will consist of plastic scintillator and water to allow the separate determination of exclusive neutrino cross-sections on carbon and on water.

- Electromagnetic calorimeter (ECAL): Surrounding the P0D and the tracker is an electromagnetic calorimeter. The ECAL is a segmented Pb-scintillator detector whose main purpose is to measure those γ-rays produced in ND280 that do not convert in the inner detectors and is critical for the reconstruction of π^0 decays.

- Side Muon Range Detector (SMRD): Air gaps in the sides of the UA1 magnet are instrumented with plastic scintillator to measure the ranges of muons that exit the sides of the ND280. The SMRD also can provide a veto for events entering the detector from the outside and a trigger useful for calibration.

In addition to these detectors which will be set at off-axis of neutrino beams, the on-axis neutrino monitor (N-GRID) will be set to directly measure the direction of the neutrino beam.

3.2 Neutrino experimental hall

The neutrino experimental hall is called the ND280 hall (the neutrino detector hall at 280m from the target point). The location of the ND280 hall is shown in Figure 3.2. The ND280 hall is being designed as follows, which is drawn in Figure 3.3.

The ND280 hall has a pit with a diameter of 17.5m and a depth of 37m, which incorporates both the on-axis and off-axis detectors. The B1 floor, which is about 24m deep, is for the off-axis detector. The off-axis detector is nearly located on the line between the target point and the SK position. The B2 floor, which is about 33m deep, is for the horizontal part of the on-axis detector. The B3 floor, which is 37m deep, is for the deepest part of the vertical on-axis detector. The exact location of the on-axis detector N-GRID will be fixed for the nominal off-axis angle $2.5\mathrm{deg}$ and the horizontal units of N-GRID will be set on the B2 floor. This facility design can accommodate with the off-axis case of $2.0 - 2.5$ degrees with the condition that the on-axis detector covers the ± 4m area.

The hut with a size of 21m $\times$ 28m covers the pit, and has a 10ton crane. The effective height of the crane is 5m. There is an area in the hut for the unloading of detector components and for the detector preparation. Some area in the hut at the ground floor is used for the electricity preparation and the cooling water preparation.

The construction of the ND280 hall and the installation of the detectors will be done in the following steps starting in Spring 2007.

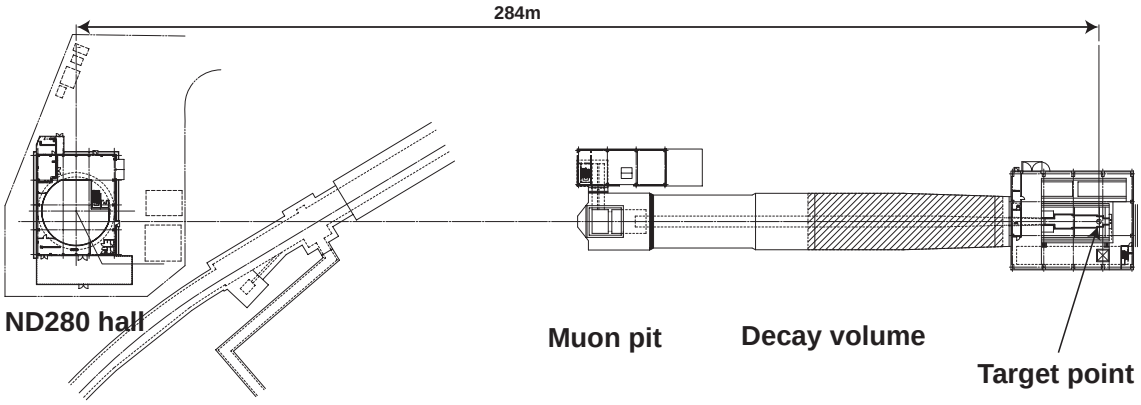

Figure 3.2: Location of the muon pit and the ND280 hall.

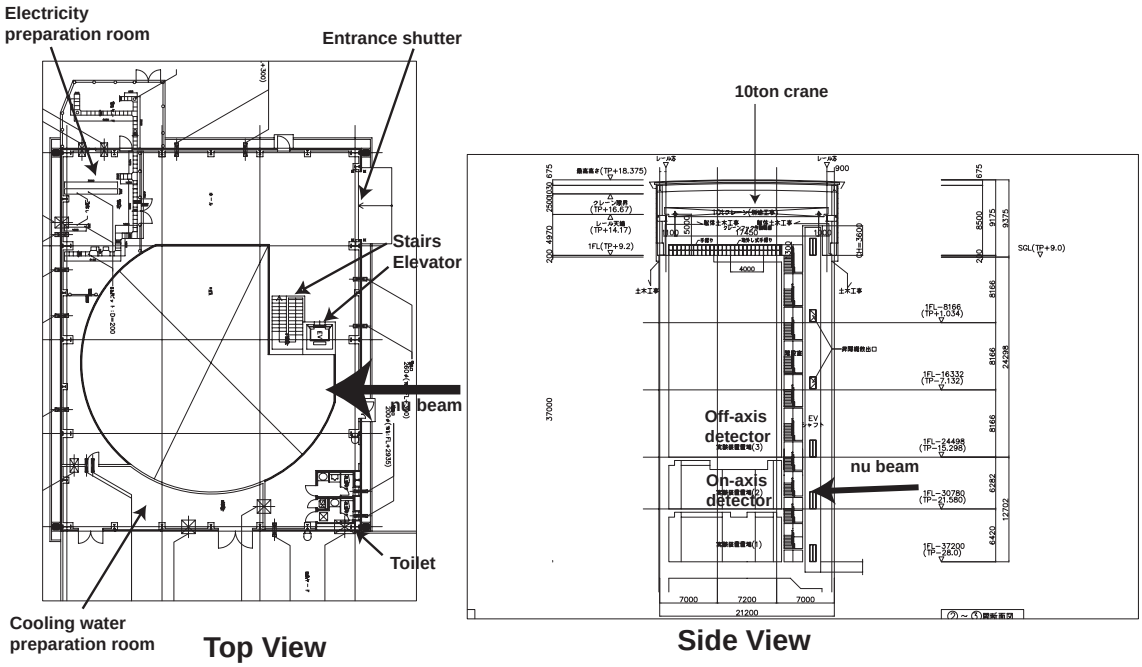

Figure 3.3: Current design of the ND280 hall.

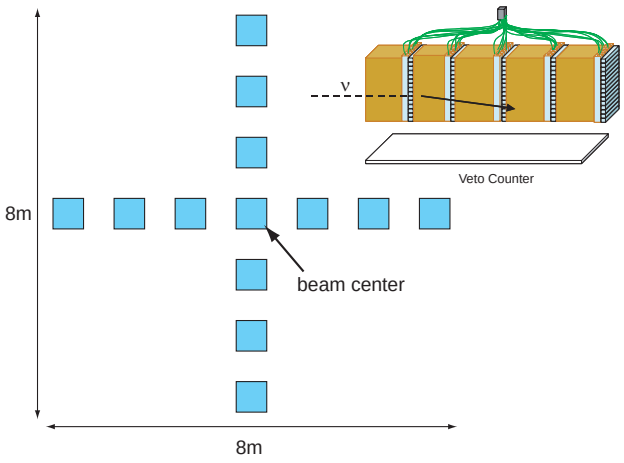

Figure 3.4: The arrangement of N-GRID detectors at the near detector hall.

1. The excavation of the pit.
2. The construction of the underground floors.
3. The installation of the magnet yokes and coils using external cranes.
4. The construction of the hut including the 10ton crane.
5. The installation of the on-axis detector.
6. The installation of the off-axis detector.

3.3 The on-axis neutrino monitor (N-GRID)

The muon monitor observes only the small fraction of muons which have energy greater than 5 GeV. Therefore, it is also important to directly measure the direction of the neutrino beam. The on-axis neutrino monitor (N-GRID) will be installed in the near detector hall to measure the neutrino beam direction and profile using neutrinos directly. It is required to measure the neutrino beam direction with precision much better than 1 mrad as for MUMON.

The neutrino event rate around the beam center is estimated to be ~ 0.3 events/ton/spill. In order to monitor the stability of the neutrino event rate (direction) at the 1% (1 mrad) precision within a single day ($\simeq 2.5 \times 10^4$ spills), $\mathcal{O}(1)$ ton fiducial mass is necessary for the detector. In addition, the variation of the efficiency of the detector across the beam profile should be calibrated at a precision of 1% during the experiment.

The N-GRID detector is designed to consist of $7+7$ identical units, arranged to form a grid which samples the beam on $8 \times 8\mathrm{m}^2$ ($\pm 4\mathrm{m} \times \pm 4\mathrm{m}$) area, as shown in Figure 3.4. The design of one unit which was made as a prototype is shown in Figure 3.5. For N-GRID, the target of neutrino interaction is iron, and the scintillators are used to detect a muon from the interaction.

3.4 Magnet

The UA1 magnet is presently stored at CERN, and the CERN Council has approved its donation to the T2K experiment. The magnet will provide a horizontal uniform field of 0.2 T, perpendicular to the neutrino beam direction over an inner volume of 88 m^3. A schematic drawing of the magnet, placed on its support structure, is shown in Figure 3.6 and the specification is summarized in Table 3.1.

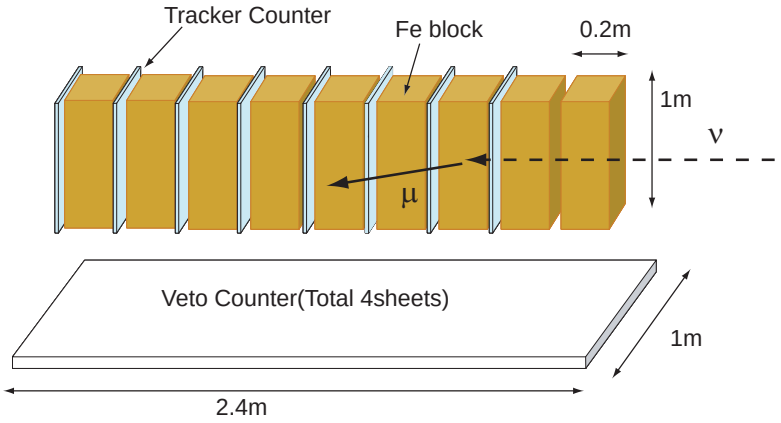

Figure 3.5: The drawing of the N-GRID prototype detector tested in the K2K experiment. The thickness of the iron block is 20 cm in the prototype. The thickness of the iron block for the real detector is 10cm optimized for the T2K beam.

Figure 3.6: The UA1 magnet.

Magnetic field	0.2 T (maximum field 0.67 T)
External dimensions	7.6 m(L), 6.1 m(H), 5.6 m(W)
Internal dimensions	7.0 m(L), 3.6 m(H), 3.5 m(W)
	(Inner volume $\sim 88m^3$)
Iron yoke weight (16 C)	850 tons
Coils material	Aluminum
Number of turns	208
Number of double pancakes	26
Total conductor weight	31 tons
Ohmic resistance (at T = 40^0 C)	0.0576 Ω
Inductance	0.36 H
Nominal current	3000 A (for B = 0.2 T)
Power dissipation	0.6 MW (for B= 0.2 T)
Cooling water flow in coils ($\Delta T = 10^0 C$)	15 liter/sec

Table 3.1: Specification of the magnet.

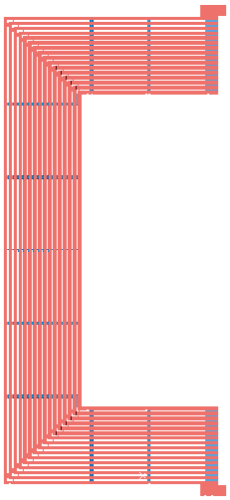

Figure 3.7: Lateral view of one of the 16 C's composing the iron yoke.

The magnet consists of two halves which are mirror symmetric about a vertical plane containing the beam axis. Each half consists of 8 C-shaped flux return yokes, made of low-carbon steel plates. The 16 C's forming the yoke have all a very similar structure. Figure 3.7 shows that the C is segmented in 12 azimuthal sections. Each section is made of 16 iron plates 5 cm thick, with 1.7 cm air gap between plates. Apart from the corners, the plates at different depth have the same size. Their dimensions are $0.88 \times 0.90\mathrm{m}^2$ (vertical plates) or $0.88 \times 0.70\mathrm{m}^2$ (horizontal plates). In the UA1 experiment the gaps between plates were instrumented with scintillators and the iron yoke acted as hadron calorimeter. We plan to put scintillators in the gaps to identify laterally escaping muons and to measure their range (Side Muon Range Detector, SMRD).

It will be possible to move the two halves apart by 5.5 meters, so to guarantee easy access for the assembling of the inner detector (the maximum transverse dimension of the inner detector is 3.5 meters).

For the assembling of the inner detector inside the magnet, we plan to adopt a technique similar to that of the NOMAD experiment, but to use a newly designed framework, adapted to our detector. With the possible exception of the electromagnetic calorimeter (which could be divided in two halves

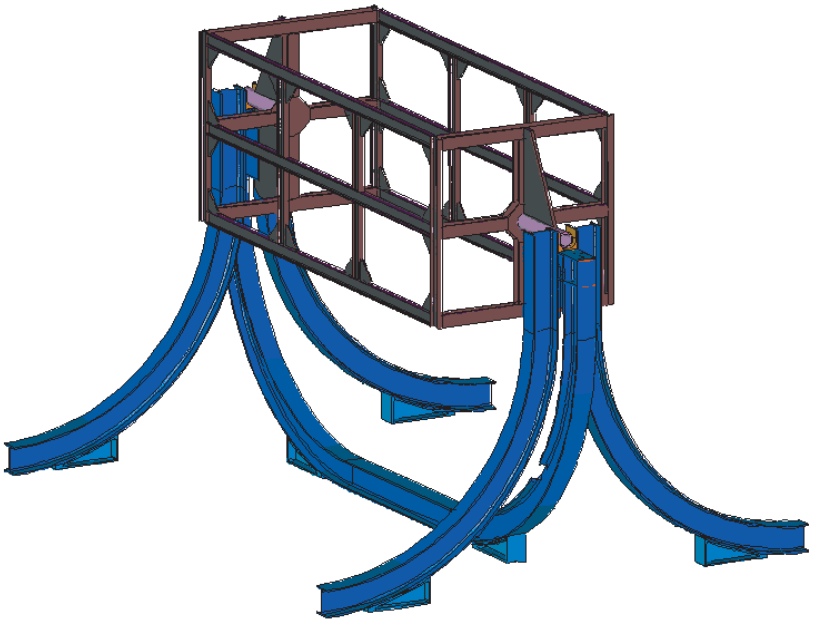

Figure 3.8: Preliminary drawing of the basket.

and fixed to the iron yokes), all other detectors will be assembled inside a metallic frame ("basket") with approximate dimensions of $6.5 \times 2.6 \times 2.5\mathrm{m}^3$. A preliminary design of the basket with its supporting structure is shown in Figure 3.8. The basket will be completely open at the top, to allow the insertion of the various detectors. Two short beams will be fixed at the center of the two faces of the basket perpendicular to the beam axis. The short beams will be connected outside the magnet to a structure fixed on the floor, which holds the basket. The beams will connect the basket to the external support structure passing through the holes in the coils , originally designed to allow the passage of the beam pipe. When opening the magnet, the C's and the coils move apart, while the basket and the inner detector remain in the position chosen for data taking. The design and construction of the basket and of the supporting structures, can be accomplished in less than one year. Therefore, we shall wait for the final engineering design of the inner detectors before to finalize the design of these structures.

3.5 TPC

Three identical TPC modules in the shape of rectangular boxes as shown in Figure 3.9 are installed in the basket. The outer dimensions of each module are assumed to be approximately 2.5 m $\times$ 2.5 m in the plane perpendicular to the neutrino beam direction, and 0.9 m along the beam direction. The transverse dimension is chosen to provide space between the inner wall of the magnet and the TPC modules for electromagnetic calorimeter and for a mechanical support cage. The dimension along the beam direction is chosen to achieve the required momentum resolution, including the necessary inactive elements.

Diffusion of the drifting electrons can be a limiting factor in the intrinsic space point resolution of a TPC. A simple upper bound on the diffusion can be calculated using the standard Gluckstern parameterization, assuming a large number of measurements along the length of the track,

$$D < \frac{\sigma_{p_t}}{p_t}\sqrt{\frac{n_T L}{720}}(L[m])^2\frac{0.3B[T]}{p_t[GeV/c]}\frac{1}{\sqrt{L_{\mathrm{drift}}}} = 260\ \mu\mathrm{m}/\sqrt{\mathrm{cm}}, \tag{3.2}$$

by demanding that the diffusion component of the momentum resolution is less than 5% at $p_t =$

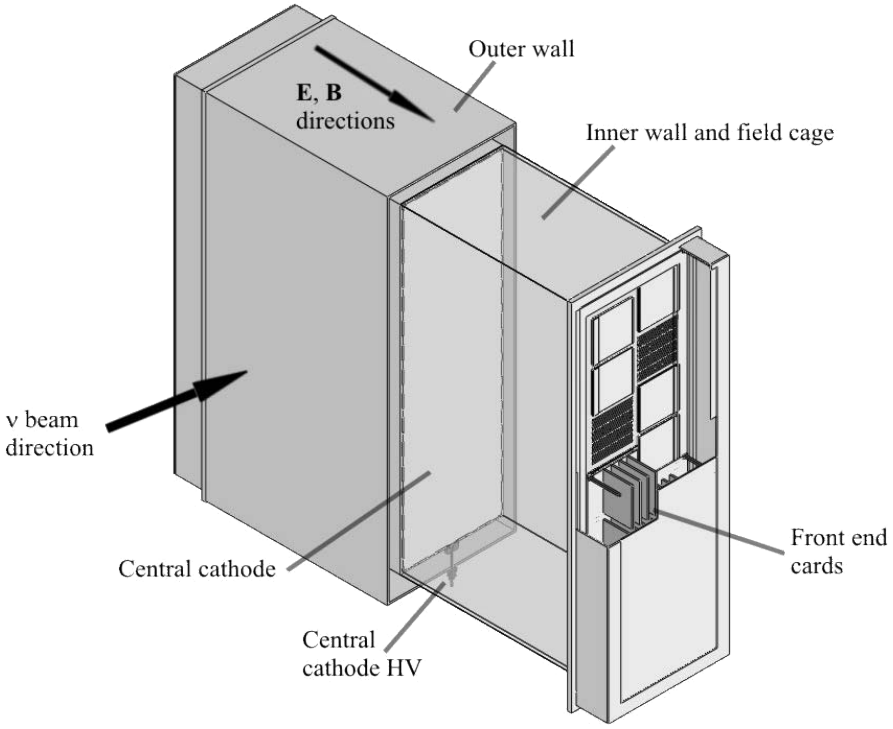

Figure 3.9: The schematic view of TPC.

1 GeV/c, and assuming $n_T = 90$ ionization electrons per cm of gas (argon) for a track measured over $L = 60$ cm after drifting for a distance, $L_{\rm drift} = 125$ cm.

Gas components under consideration include Argon, Neon, CO_2 methane, iso-butane, and CF_4. A candidate for the T2K TPC gas mixture is Ar CO_2 (90:10). At a drift field of 200 V/cm, the transverse diffusion is approximately 220 $\mu{\rm m}/\sqrt{\rm cm}$ and the drift velocity is 14 mm/μs. Higher concentrations of CO_2, 20-30%, reduce the diffusion constant further, in the range of 150 $\mu{\rm m}/\sqrt{\rm cm}$ although this requires higher drift fields, up to approximately 400 V/cm. Ar CF_4 (97:3) is another possible gas candidate. It is very fast, but saturates near 200 V/cm, and therefore is more stable against gas density fluctuations.

To operate the TPC at drift fields up to 400 V/cm with a maximum drift length of 1.25 m, the central cathode potential will be at most 50 kV. In order to limit the development time for the TPC field cage and gas containment vessel, the designs of existing TPCs were considered in detail, in particular those of ALEPH, NA49, STAR, and ALICE. A preliminary T2K TPC design concept that most resembles the STAR design has been chosen, in order to achieve a very uniform drift field without high surface fields and whose structure is rigid and relatively easy to construct.

The T2K TPC field cage volume and endplates are surrounded by a separate CO_2 gas envelope, to provide safe insulation between the central cathode and the outer wall of the TPC, and to reduce contamination from O_2, N_2 and water from the atmosphere into the drift volume. The gas gap is 75 mm thick. The walls of the inner and outer gas volumes are made of composite material, with a rohacell core and thin copper clad G10 skins. The walls, about 20 mm thick, are constructed as flat panels and then assembled into rectangular box structures, with tongue-in-groove and glue joints. The central cathode will also be constructed by the same technique, and will be positioned and held in grooves cut into the field cage walls. Perforations or gaps around the edge will allow gas to mix on both sides of the cathode.

Proposed baseline design uses either GEMs or Micromegas for the gas amplification.

Figure 3.10: The prototype TPC.

GEM foils measuring 30 cm $\times$ 30 cm that follow the design used in the Compass experiment [29] can be used to build readout amplification modules that are joined together into sectors and inserted into the field cage endplate. Three GEM foils are used in each readout module, in order to safely achieve good gas gain of a few thousand. Potential suppliers of large GEM foils include the CERN PCB shop and two private companies, 3M and TechEtch. The GEM foils are placed on thin fiberglass frames, with narrow spacer strips to maintain the gap between neighboring GEM foils.

Similarly, large Micromegas foils could be used to build the readout modules. Today, the largest microchannel devices in operation are the 40 $\times$ 40 cm^2 Micromegas modules of Compass [30]. Large surface Micromegas detectors can be realized with a woven mesh (produced for instance by Gantois) of 38 μm thickness. A promising technique to build these modules is "Micromegas in the bulk" [31], where the mesh is sandwiched between two resistive "Vacrel" layers. This leads to mechanically robust detectors and there is no need of an external frame to hold the mesh. Possible furnishers of these detectors are the CERN PCB shop and the SEDI (Dapnia, Saclay) laboratory.

Prototype TPC was built as shown in Figure 3.10 with which various tests are being performed. We tested two technologies and proved that both worked well. So the T2K collaboration will make the decision to select one technology by July 2006.

3.6 FGD

The ND280 detector will contain two fine-grained detectors (FGDs), each with dimensions of 200 cm $\times$ 200 cm $\times$ 30 cm (scintillator volume only, not including supports or electronics). One FGD will consist of x-y layers of plastic scintillator bars read out with wavelength-shifting fibers, similar to the SciBar detector [32]. The second detector will be a water-rich detector, will consist of x-y layers of plastic scintillator alternating with 3 cm thick layers of water.

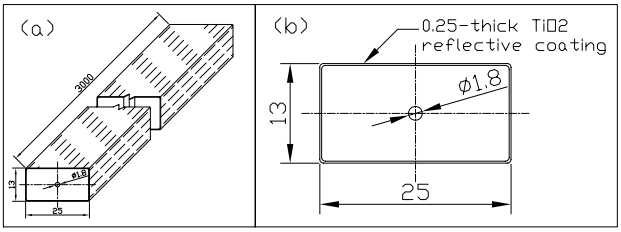

Figure 3.11: A drawing of the scintillator strip used for the K2K SciBar detector. The scintillator has a hole in the middle, and the surface is covered by TiO_2 reflective coating.

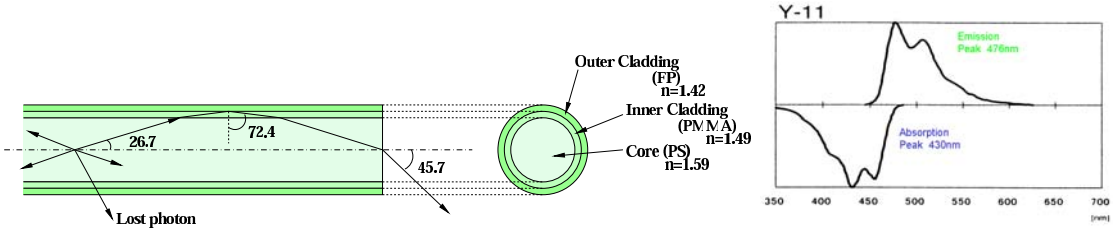

Figure 3.12: (Left) Drawing of the Y11 double-clad WLS fiber. (Right) Absorption and emission spectra of the Kuraray Y11 WLS fiber.

The size of the scintillator bars for the plastic FGD is $1.0 \times 1.0 \times 200$ cm^3, and the surface is covered by TiO_2 reflective coating. Each scintillator bar has a hole in which a wave-length shifting (WLS) fiber is installed. As an example, the drawing of the scintillator bar used for SciBar is shown in Figure 3.11. The extruded scintillator is planned to be produced in Canada with co-extrusion technique of the reflective coating.

The detector size is $200 \times 200 \times 30$ cm^3 resulting in the total mass of 1.2 tonnes, which does not include supports or electronics. One layer consists of 200 scintillator bars, and thirty layers are arranged in alternating vertical and horizontal layers perpendicular to the beam direction. The tracking threshold is expected to be ~ 4 cm, which corresponds to 350 MeV/c for a proton.

Kuraray Y11 wave-length shifting (WLS) fibers are used for light collection and light propagation. The absorption and emission spectra of Y11 are shown in Figure 3.12. The absorption spectrum of WLS fiber is well matched with the emission spectrum of the extruded scintillator ($\sim$ 420 nm). Double-clad WLS fiber is adopted to increase the light collection efficiency. The drawing of the double-clad fiber is shown in Figure 3.12

The water-rich FGD consists of x-y layers of scintillator bars alternating with 3 cm thick layers of water (no readout). These water layers will be constructed from sheets of corrugated polypropylene, of dimension 1.0 m x 2.0 m, and an outer thickness 1.0 cm. These are commercially available. The total water content is 47% by weight.

Neutrino interaction rates on water can be obtained from a subtraction analysis in which the rates on the all-plastic FGD and the water-rich FGD are measured, corrected for any differences in efficiency, and then the interaction rates on carbon determined from the plastic FGD are subtracted from the plastic+water FGD to get the interaction rate for just water.

3.7 P0D

The P0D is a solid scintillator strip detector using water to provide a large oxygen content, which is based on K2K SciBar experience and MINERνA design, and is instrumented target region surrounded by an electro-magnetic calorimeter as shown in Figure 3.1.

Scintillating bar tracking planes are the primary component of the P0D. The baseline design has

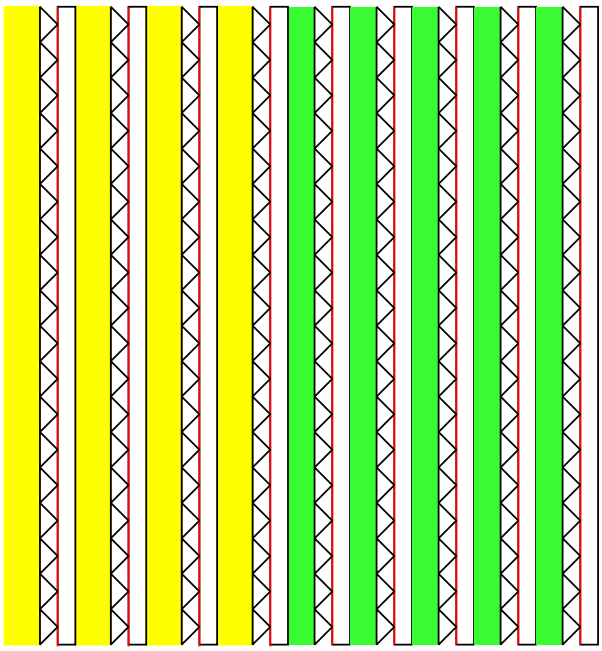

Figure 3.13: The schematic view of assembled P0D layers. White shows extruded scintillators; red shows lead foil; yellow shows water cell; green shows polypropylene plate

76 tracking planes position perpendicular to the beam direction. The tracking planes are constructed of polystyrene triangular scintillating bars that are fabricated by co-extruding with a reflective layer TiO_2 and a central hole for a WLS fiber. The nominal bar has a 3 cm base and a 1.5 cm height and has a length of 180 cm or 210 cm. Tracking planes have thin layer of lead (nominally 0.06 cm) sandwiched between X and Y layer of interlocked scintillating bars to increase the efficiency to detect gamma rays from π^0 decay. The light seal for the tracking plane is maintained by light manifolds which collect the WLS fibers into the photo-sensors. Figure 3.13 shows the schematic view of the assembled P0D layers.

One of the constraints facing the P0D is that the neutrino interactions must be measured on a oxygen target. In the baseline design, this is achieved by interleaving water target planes between the 30 upstream scintillating bar tracking planes. Oxygen cross section measurements will be made by comparing the interaction rate for events vertices in the upstream and downstream portions of the detector. The water cells consist of semi-flexible pillow bladders, nominal dimensions 3 cm $\times$ 1.8 m $\times$ 2.1 m, holding about 100 kg of water each. They are provided with fill tubes at top and drain tubes at bottom. The drain tubes will run through a simple manifold outside the magnet, and thus serve as sight tubes for checking water levels. The bladders are made from rubberized cloth or polyethylene-coated EVAL plastic.

The detector has a total mass of approximately 12 tons with a fiducial mass of 1.7 tons of water, 3.6 tons of plastic scintillator, and 0.8 tons of lead. Based on the expected event rates, we expect to collect a total sample of approximately 60,000 neutral current single-π^0 events for an exposure of 10^{21} POT (approximately one year), of which approximately 17,000 occur in the water target.

3.8 ECAL

The purpose of the electromagnetic calorimeter (ECAL) is to capture and characterize electromagnetic energy produced by neutrino interactions in the inner detectors (the P0D, the FGD, and the TPC), primarily photons produced by the decay of NC- or CC- produced π^0. The ECAL also acts as an active veto detector, shielding the internal detectors from particles produced by neutrino interactions in the magnet or other surrounding material.

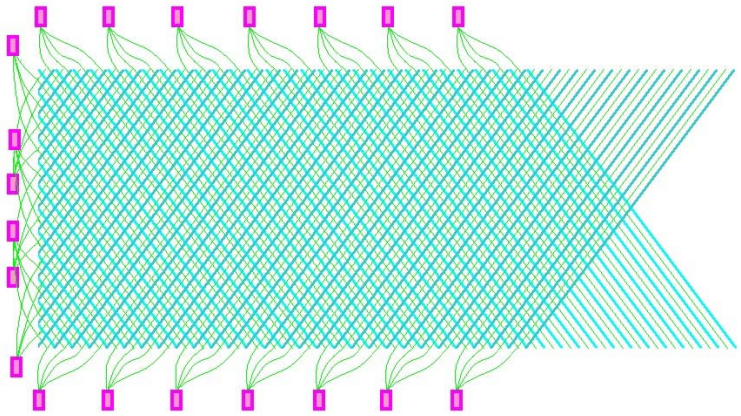

Figure 3.14: Sketch of the layout of the bars for a UV projection for ECAL. Readout could be either single-ended or two-ended with (hopefully) no additional space needed at the sides.

We plan to add a "pre-radiator" section into the ECAL in an attempt to produce more elongated photon "showers" (at these relatively low energies photons have a very significant Compton scattering cross section, meaning that they do not "shower" so much as multiply scatter), which hopefully will provide more accurate tracking information. The basic components are 3 mm thick Pb alloy sheets and 1 cm thick $\times$ 5 cm wide plastic scintillator bars (with signal readout by optical fiber, as with most of the rest of the subdetectors in the ND280 detector). The "ECAL" section consists of 15 layers, each of which has one sheet of Pb alloy and one layer of scintillator bars. Interior to this section is the "pre-radiator" section, where each of the 3 layers consists of a sheet of Pb alloy backed by 3 layers of plastic scintillator bars. Scintillator bars will be configured in UV alignment as shown in Fig3.14. This configuration has the advantage that all the bars are the same (shorter) length, (minimizing problems with photon attenuation), thereby perhaps allowing single-ended readout, and position resolution along the beam direction (z-axis) is as good as x and y-axises.

In terms of mechanical support for the ECAL, all ECAL sections would be fixed to the magnets and would open and close with them (so the top and bottom would be divided in half on the magnet center-line). The top would hang from the magnet (through the gaps in the coil), the bottom would sit on the magnet (once again through the coil gaps), while the side sections would be mounted on the magnet. Detailed engineering design of these supports is ongoing.

3.9 SMRD

The magnet iron yoke consists of 16 C-shaped elements as shown in Figure 3.7. Each C is made of sixteen 5 cm thick iron plates, with 1.7 cm air gaps between the plates, and is segmented in 12 azimuthal sections. The SMRD will be build with these iron plates and scintillator equipped into the air gaps (88$\times$ 80$\times$1.7 cm).

The muon momentum distribution for CC-QE interactions that hit the SMRD is shown in Figure 3.15. The vast majority of large angle muons, namely 91% of all muons not escaping in the forward direction (e.g. $\cos\theta < 0.8$) have momenta of less than 600 $\mathrm{MeV/c}$. Since the iron plates in the yokes are approximately 5 cm thick, it would be sufficient to instrument 6 to 7 radial layers in order to completely range out 95% of all muons that are not escaping in the forward direction. Table 3.2 lists the range of muons in iron and the corresponding number of layers as functions of energy, along with the fraction of muons that is represented.

The Monte Carlo study [34] indicates that a muon energy resolution of less than 10% can be achieved. As expected, the energy resolution is best for muons emitted at large angles (e.g. perpendicular to the beam direction) and worsens for muons emitted at smaller angles with respect to the beam direction.

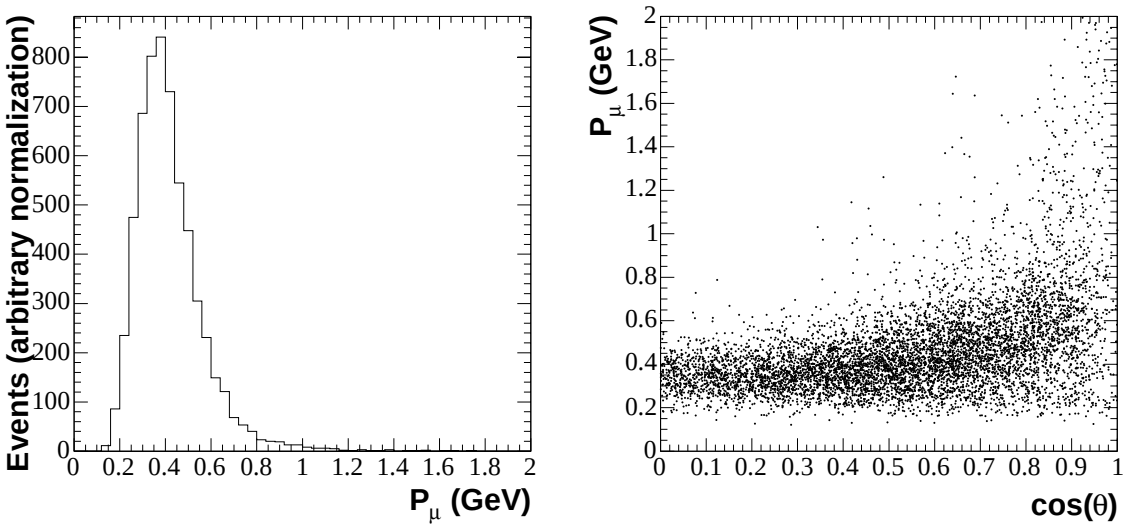

Figure 3.15: Left plot: muon momentum for CC-QE muons reaching the SMRD with $\cos\theta < 0.8$. Right plot: muon momentum for CC-QE muons reaching the SMRD versus $|\cos\theta|$.

P_μ^{max} (GeV)	$f(\%)$	Range (cm)	Layer
0.5	79	24	5
0.6	91	31	6
0.7	96	37	7
0.8	98	44	9
0.9	99	51	10
1.0	99	57	12
1.1	100	65	13

Table 3.2: Maximum detected muon momentum and corresponding fraction f of muons originating from CC-QE reactions with $|\cos\theta| < 0.8$. The penetration depth in iron and the corresponding number of layers in the SMRD are specified in the two right-hand columns.

Figure 3.16: The left and right panel show a 87 cm long, 17 cm wide, and 1 cm thick scintillator with grooves to embed WLS fibers. The spacing between the grooves is 2.5 cm. The scintillator shown in the right panel is coated with a chemical reflector.

In order for the ND280 detector to reliably identify CC-QE interactions and identify background events originating from the cavity and the iron yokes themselves, the SMRD is required to identify minimum ionizing particles (MIP) with very good efficiency. Hence the active detector medium has to provide uniform and high light yield. It is also desirable to have good inter-layer timing resolution to distinguish inward- from outward-going particles.

The active component of the SMRD will consist of slabs of 1 cm thick plastic scintillator which will be sandwiched between the iron plates of the magnet yokes. Equidistant wavelength shifting fibers will be embedded into the scintillators in order to achieve good light yield and consequently high detection efficiencies of traversing minimum ionizing particles (MIP). A prototype scintillator-WLS configuration shows the MIP detection efficiency is more than about 99.5%.

The WLS fiber will also serve to guide the light into the photo-detectors. The fibers can be read out on both sides. The scintillators will be coated with a chemical reflector to enhance the light yield. Figure 3.16 shows a 87$\times$17$\times$1 cm slab of extruded scintillator with grooves for future insertion of WLS fibers. The left and right panel show the plastic before and after the application of a chemical reflector coating. The grooves are spaced at 2.5 cm. The WLS fibers will be bend inside the scintillator with a radius of 3 cm to allow the fibers to exit parallel to the gap in between iron yokes. This setup aims to minimize the mechanical exposure of the sensitive fibers inside the inter-yoke gaps and naturally prevents the fibers from being buckled.

The mechanical implementation of the SMRD will allow access to each scintillator slab after the start of the experiment, so that repairs and adjustments can be accomplished. It is planned to place the scintillator slabs into thin aluminum drawers. Each of the drawers will fit into a gap in the iron yokes and individual drawers will be connected to each other with flexible but sturdy spacers. This will allow installation and access for repair to all scintillator slabs despite the limited detector access space and space constraints imposed by the iron yokes. Figure 3.17 shows a sketch of such a drawer configuration. The drawers provide mechanical stability and will also serve to protect the light tight wrapping from tear during installation and potential maintenance retrieval.

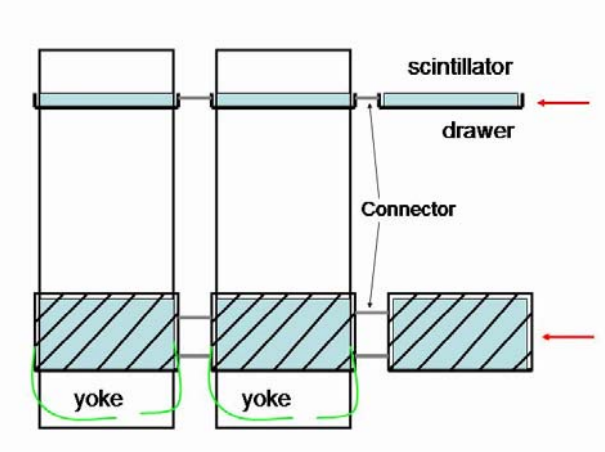

Figure 3.17: Illustration of the drawer system which will allow deployment and retrieval of the scintillator slabs.

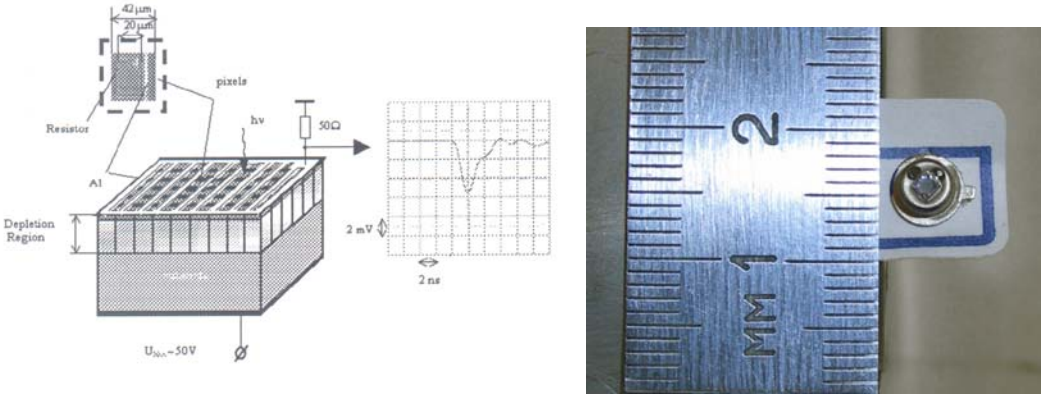

Figure 3.18: (Left) multi-pixel semiconductor photodiode view. (Right) Photo of a multi-pixel semiconductor photodiode. Diameter of the cylindrical container is about 3 mm.

3.10 Photo Sensor

Detailed description of the avalanche photo-diodes with metal-resistor-semiconductor layer-like structure operating in the Geiger mode [35] technique can be found in [36, 37, 38, 39]. This detector is a multi-pixel semiconductor photodiode which consists of pixels on common substrate. We will use this new kind of photo sensors for FGD, P0D, ECAL, SMRD and N-GRID with Kuraray Y11 wave-length shifting (WLS) fibers.

The view of a sensor is shown in Figure 3.18. Each pixel operates as an independent Geiger micro-counter with a gain of the same order as a vacuum photomultiplier. Geiger discharge is initiated by a photoelectron, thermally or by high electric field. Gain is determined by the charge accumulated in pixel capacitance: $Q_{pixel} = C_{pixel} \cdot \Delta V$, where ΔV is the difference between the bias voltage and the breakdown voltage of the diode (overvoltage). Since ΔV is about a few volts, $C_{pixel} \simeq 50$ fF, then $Q_{pixel} \sim 150$ fC that corresponds 10^6 electrons.

A single pixel signal does not depend on a triggered number of carriers in a single pixel. In such a way, the signal is a sum of fired pixels. Each pixel operates as a binary device, but the sensor on the whole is an analogue detector with the dynamic range limited by a finite number of pixels.

The absolute gain depends on the sensor topology and bias voltage. Typical values are in the range $(0.5 - 1.0) \times 10^6$. The photon detection efficiency (ε) consists of 3 components as $\varepsilon = QE \cdot \varepsilon_{Geiger} \cdot \varepsilon_{pixel}$, where QE is the wavelength dependent quantum efficiency, ε_{Geiger} is the probability for a photoelectron to initiate the Geiger discharge, ε_{pixel} is a fraction of total active area occupied by

sensitive pixels. Measured QE is shown in Fig. 3.19 as well as the emission spectrum of the WLS fiber Y11(150). Peak emission of the fiber depends on its length due to light absorption while the

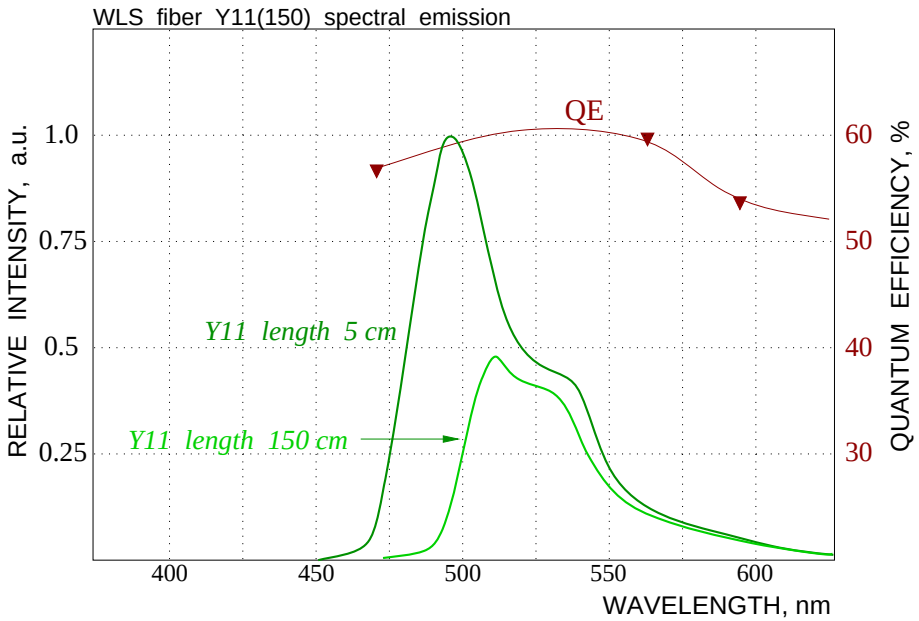

Figure 3.19: Light emission spectrum of Y11(150) fiber and the quantum efficiency of the sensor.

sensitivity is almost flat for green light. ε_{Geiger} depends on applied bias voltage and comparable with QE, ε_{pixel} is determined by topology, its typical value is about 40-60%.

Single photoelectron resolution was checked with a blue LED. The light from this LED was directed to a sensor through the short Y11 fiber. Fig. 3.20 shows the spectrum of the LED flash. Resolution here is determined by electronic noise of fast amplifier and pick-up noise produced by cabling, ground loops, etc. Intrinsic gain stability of sensor allows us to see the ADC signal with separated peaks which correspond 1, 2, 3... pixels.

We will develop the photo-sensor with a Russian company (CPTA) and a Japanese company (HPK). These new devices are successfully tested at KEK-PS (T853) and we are convinced that the new devices satisfy our requirement. We plan to have the first production proto-type in our hand by the end of 2006.

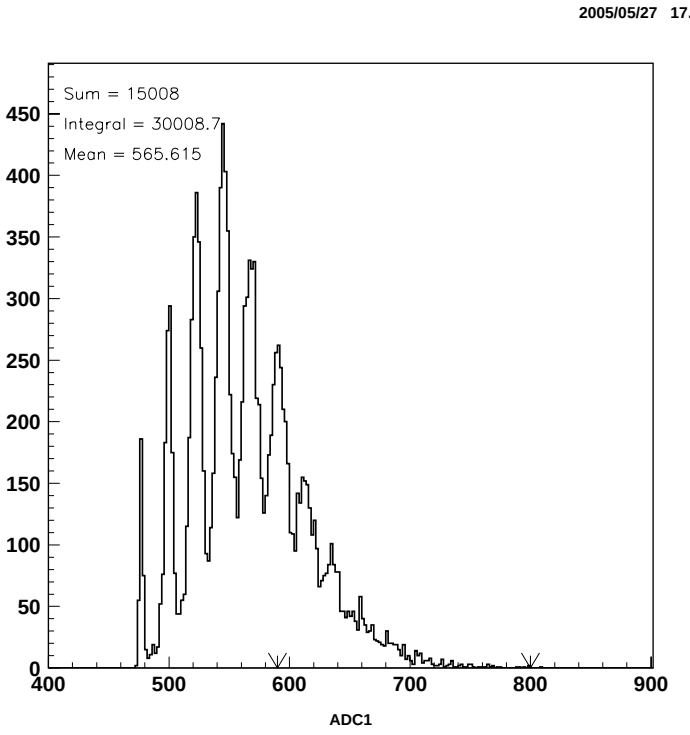

Figure 3.20: ADC spectrum of LED flash of low amplitude.

Chapter 4

Commissioning

4.1 Neutrino beam commissioning

Although the detailed commissioning plan is yet to be worked out from now, some critical items in commissioning can be listed based on previous experience in the K2K experiment and other experiments.

The goals of the commissioning include

- Ensure all the components are working as designed
- Tune primary proton beam
- Optimize targeting (position, direction, focusing)
- Understand behavior and tune secondary beam (direction)

At least the following modes of accelerator operation will be necessary from the commissioning phase to the normal operation mode.

1. Single shot, single or two bunch with 1% proton/bunch intensity (~ 0.1% intensity/spill).
2. Single shot, single or two bunch with 1% proton/bunch intensity (~ 0.1% intensity/spill). The filled bunch is changed from 1st to 9th bunch.
3. Single shot, 9 bunches with 1% proton/bunch intensity (~ 1% intensity/spill).
4. Periodic (nominal repetition), single or two bunch with 1% proton/bunch intensity (~ 0.1% intensity/spill).
5. Normal mode: Periodic (nominal repetition), 9 bunch with intensity from 1% to 100%.

In April 2009, the first beam will be on target. The first operation will be in the Mode 1 above and move to the next mode step-by-step after confirming everything is OK.

All the proton monitors, CT (intensity), ESM (beam position), SSEM (profile) will be used for beam diagnosis and tuning in the low intensity ($\lesssim 1$%) run. At higher intensity, SSEM can not be exposed to the beam all the time due to beam loss and foil aging, but can be for limited number of spills. It can be confirmed that the beam profile is changed or not when beam intensity is increased using SSEM data. Muon monitor and on-axis neutrino detector must be working from the beginning. Those detectors are necessary to optimize and monitor targetting and neutrino beam (direction).

The followings are possible measurement items during beam commissioning.

- Scan beam position, size and direction on target. This is for optimization of targetting efficiency, for understanding horn focusing and so on.

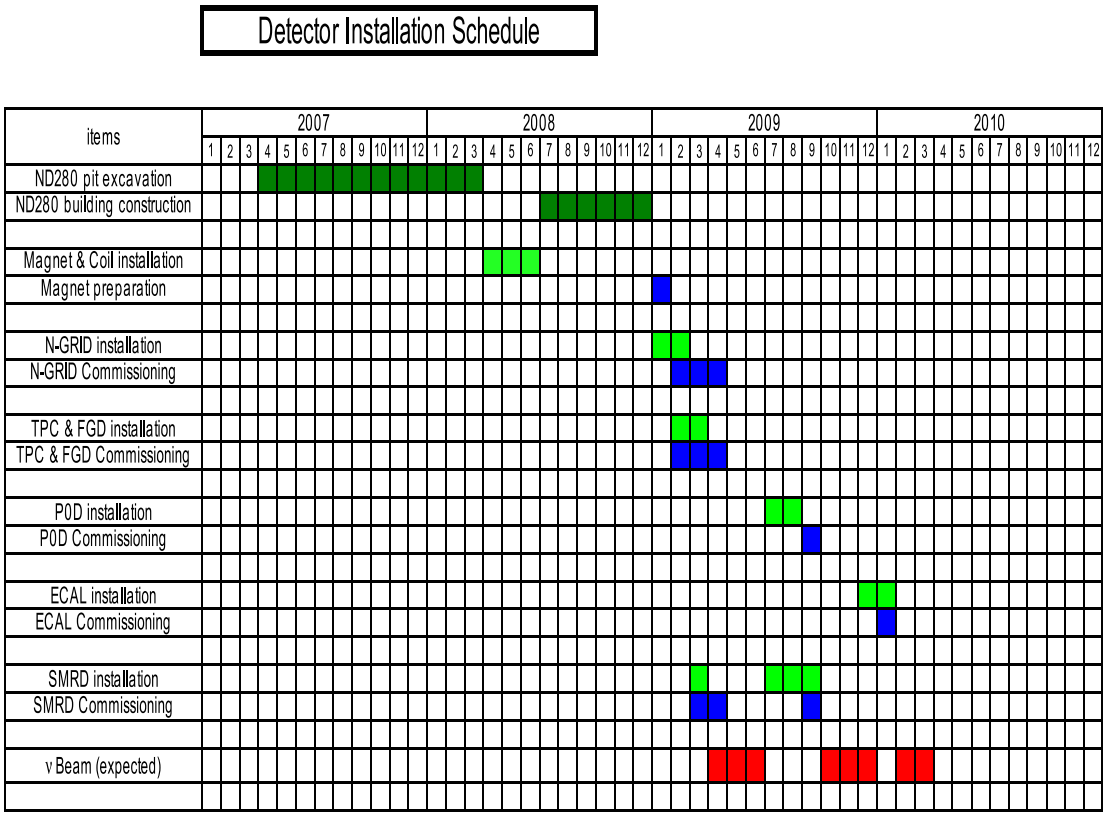

Figure 4.1: Time schedule of the off-axis and on-axis detectors.

- Horn current scan. By measuring beam profile, intensity at muon monitor and/or on-axis detector, this will provide information on beam direction at different energy component, horn collection efficiency, horn alignment and so on.

4.2 ND280 commissioning

Figure 4.1 shows the current plan of ND280 detectors. The construction of the ND280 facility will start at the beginning of Apr. 2007. The pit excavation and the construction of the underground floors will be completed by Mar. 2008.

The magnet will be installed on the underground floor B1 before the ND280 building construction, which will start in July 2008 and will be finished in 2008. From Jan. 2009, we will install a part of detectors: N-GRID, tracker(TPC and FGD) and a part of SMRD, for commissioning with neutrino beams which will be delivered from Apr. 2009.

With this partial ND280, we can measure the neutrino beam direction by the on-axis neutrino monitor N-GRID to give important information for neutrino beam line operation, and also can perform measurement of ν_μ and ν_e spectrum by the tracker via CCQE interactions.

Following the commissioning for three months with the partial ND280, we will install P0D and remaining SMRD during a break in 2009 summer then will do data taking with the ND280(without ECAL). Finally we will install ECAL in Jan.2010 to complete ND280 and will be able to carry out measurement of γ's and π^0's with the expected ND280 performance for other reactions than CCQE, which enables us to aim the goal of T2K experiment.

Chapter 5

Expected Foreign Contributions

5.1 Expected contributions to the neutrino beam line from abroad

In the beam line, the following items are expected to be contributed from collaboration institutes abroad.

- GPS time synchronization system (U.Washington/US)
- Proton intensity monitor (CT) including readout electronics (Louisiana State U./US)
- Readout electronics for proton profile monitor (SSEM) (SNU/Korea)
- Readout electronics for beam position monitor (ESM) (U. Washington/US)
- Superconducting corrector magnet (BNL,SUNY/US)
- Quench detection system (Saclay/France)
- Vacuum chamber for most downstream proton monitors including remote maintenance mechanism (TRIUMF/Canada)
- Beam window design and manufacturing (RAL/UK)
- Baffle design and manufacturing (RAL/UK)
- Optical transition radiation detector (Canada)
- Design of target and its remote handling mechanism (RAL/UK)
- Horn design and production of 2nd horn (US)
- Beam dump design (RAL/UK)

On most of the items above, collaboration work, such as R&D, design work, prototyping and its test, has already been started. Each country has requested budget for the contributions to their funding agency. Korea and Canada have already got approval. UK already has got “seed” budget to start design work. Saclay also secured budget for quench detection system. Results of the budget request in other countries are also coming within several month.

Item	Cost
N-GRID	$ 700k
Magnet	$ 1,100k
TPC	$ 1,580k
FGD	$ 2,271k
P0D	$ 3,340k
ECAL	$ 1,447k
SMRD	$ 1,281k
Total	$11,719k

Table 5.1: Cost estimate of detectors. Costs don't include a contingency, labor or facilities. We count 100 Japanese yen as 1 US dollar.

5.2 Estimated cost for ND280 and expected contributions

Table 5.1 shows the estimated cost for the ND280 detectors. We should note that it doesn't include costs for labor or facilities which will be estimated in detail. It also doesn't prepare for a contingency. Large fraction of cost for the ND280 detectors will come from abroad.

ND280 detectors are shared by sub-groups of collaborators who are interested in the subjects for ND280. The following list shows expected nation contributions to ND280 detectors.

- N-GRID : France, Japan, Korea, Russia, Switzerland
- Magnet : France, Italy, Spain, Switzerland, UK
- TPC : Canada, France, Italy, Spain, Switzerland
- FGD : Canada, Japan, Russia, UK
- P0D : UK, US
- ECAL : UK
- SMRD : Italy, Japan, Russia, US
- Electronics/DAQ : Canada, France, Japan, Spain, UK

Figure 5.1 shows the ND280 organization, with which R&D, design and many things for ND280 detectors are being carried out.

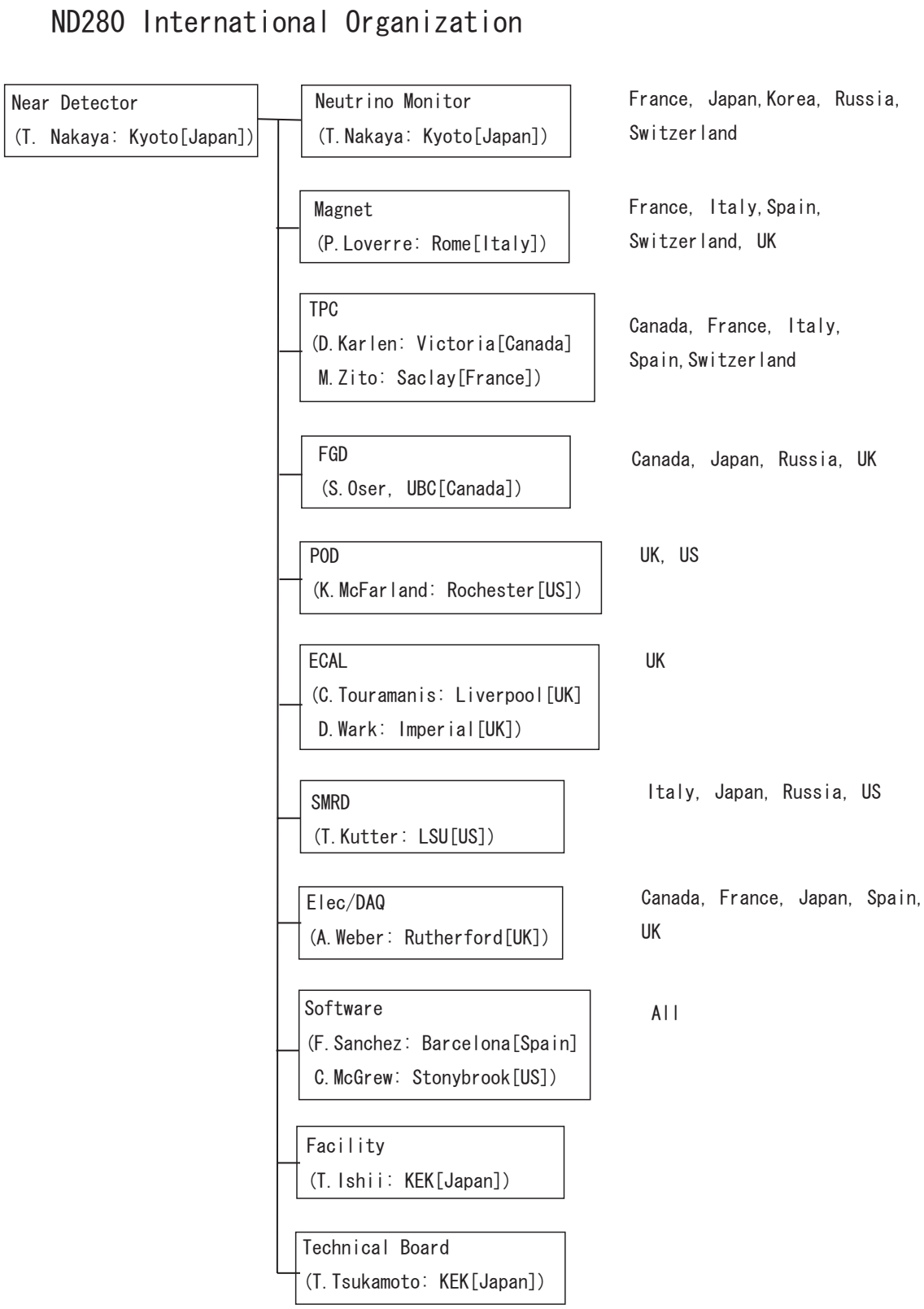

Figure 5.1: ND280 organization. Boxes show sub-groups and sub-group coordinators are shown in parentheses. Expected contributing nations to sub-groups are indicated nearby those in which they are interested.

Bibliography

[1] B. Cleveland, *et al.*, Astrophys. J. **496**, 505 (1998)

[2] Y. Fukuda, *et al.*, Phys. Rev. Lett. **77**, 1683-1686 (1996);
K.S. Hirata, *et al.*, Phys. Rev. D **44**, 2241-2260 (1991)

[3] V. Gavrin, *Results from the Russian American Gallium Experiment (SAGE)*, VIIIth International Conference on Topics in Astroparticle and Underground Physics (TAUP 2003), Seattle, September 5–9, 2003;
J.N. Abdurashitov *et al.*, J. Exp. Theor. Phys. **95**, 181 (2002);
the latest SAGE results were presented by C. Cattadori, *Results from Radiochemical Solar Neutrino Experiments*, XXIst International Conference on Neutrino Physics and Astrophysics (Neutrino 2004), Paris, June 14–19, 2004.

[4] E. Bellotti, *The Gallium Neutrino Observatory (GNO)*, VIIIth International Conference on Topics in Astroparticle and Underground Physics (TAUP 2003), Seattle, September 5–9, 2003;
M. Altmann *et al.*, Phys. Lett. B **490**, 16 (2000);
W. Hampel *et al.*, Phys. Lett. B **447**, 127 (1999)

[5] Y. Ashie, *et al.*, Phys. Rev. D **71**, 112005 (2005);
Y. Fukuda, *et al.*, Phys. Rev. Lett. **81**, 1562-1567 (1998)

[6] Q.R. Ahmad *et al.*, Phys. Rev. Lett. **87**, 071301 (2001);
Q.R. Ahmad *et al.*, Phys. Rev. Lett. **89**, 011301 (2002);
S.N. Ahmed *et al.*, Phys. Rev. Lett. **92**, 181301 (2004);
nucl-ex/0502021, submitted to Phys Rev C

[7] K. Eguchi*et al.*, Phys. Rev. Lett. **90**, 021802 (2003);
K. Eguchi *et al.*, Phys. Rev. Lett. **94**, 081801 (2005)

[8] E. Aliu *et al.*, Phys. Rev. Lett. **94**, 081802 (2005)

[9] Z. Maki, N. Nakagawa, and S. Sakata, Prog. Theor. Phys. **28**, 870 (1962)

[10] M. Kobayashi, T. Maskawa, Prog. Theor. Phys. **49**, 652 (1973)

[11] S. P. Mikheyev and A. Yu. Smirnov, Sov. J. Nucl. Phys. **42**, 913 (1985);
L. Wolfenstein, Phys. Rev. D **17**, 2369 (1978)

[12] C. Athanassopoulos, *et al.*, Phys. Rev. C542685-27081996, nucl-ex/9605001;
A. Aguilar, *et al.*, Phys. Rev. D641120072001

[13] B. Armbruster, *et al.*, Phys. Rev. D **65**, 112001 (2002);
E.D. Church, K. Eitel, G.B. Mills, M. Steidl, Phys. Rev. D **66**, 013001 (2002)

[14] E. Church, *et al.*, nucl-ex/9706011.

[15] M. Fukugita and T. Yanagida, Phys. Lett. B **174**, 45 (1986)

[16] M. Apollonio, *et al.*, Eur. Phys. J. **C27**, 331-374 (2003);
M. Apollonio, *et al.*, Phys. Lett. B **466**, 415-430 (1999).

[17] P-875: A Long Baseline Neutrino Oscillation Experiment at Fermilab, D. Ayres et al.. MINOS Proposal, NuMI-L-63. `http://www.hep.anl.gov/ndk/hypertext/numi_notes.html`.

[18] The OPERA experiment, H. Pessard, *et al.* (OPERA), hep-ex/0504033.

[19] The ICARUS experiment, a second-generation proton decay experiment and neutrino observatory at the Gran Sasso Laboratory, Arneodo, F, *et al.* (ICARUS), hep-ex/0103008.

[20] First MINOS Oscillation Results, `http://www-numi.fnal.gov/talks/results06.html`

[21] http://jkj.tokai.jaeri.go.jp/index-e.html

[22] Y. Fukuda, *et al.*, Nucl. Instrum. Methods **A**, 501 (2003)418-462

[23] D. Beavis, A. Carroll, I. Chiang, *et al.*, Proposal of BNL AGS E-889 (1995).

[24] S. Fukuda *et al.* (Super-Kamiokande Collaboration), Phys. Rev. Lett. **85**, 2000 (3999-4003)

[25] RD42 Collaboration web page, `http://rd42.web.cern.ch/RD42/`

[26] A section in Canadian proposal to their funding agency, http://jnusrv01.kek.jp/jnu/monitor/OTR/nserc_rti_v2.1.pdf

[27] R. Ishida, Talk at the T2K280m meeting, October 25, 2003.
http://www-he.scphys.kyoto-u.ac.jp/ nakaya/jparc/index.htm
http://www-he.scphys.kyoto-u.ac.jp/ nakaya/jparc/doc/ND280m_Oct25-27-2003/r_ishida.pdf

[28] S.J.Barish et al, Phys. Rev. D**19**:2521,(1979).

[29] C. Altunbas, et al., *Construction, test and commissioning of the triple-gem tracking detector for compass*, Nucl. Instrum. Methods **A**, 490 (2002)177.

[30] A. Magnon et al., *Tracking with 40x40-cm**2 micromegas detectors in the high energy, high luminosity compass experiment*, Nucl. Instrum. Methods **A**, 478 (2002)210.

[31] I. Giomataris et al., *Micromegas in a Bulk*, physics/0501003, January 2005.

[32] K. Nitta et al.,The K2K SciBar detector, Nucl. Instrum. Methods **A**, 535 (2004)147-151

[33] Minerva Collaboration, hep-ex/0405002

[34] F. Sanchez, Talk at the T2K280m meeting, October 7, 2004

[35] G.Bondarenko,V.Golovin, M.Tarasov, Patent for invention in Russia No. 2142175, 1999.

[36] G.Bondarenko et al., Nucl. Phys. Proc. Suppl., 61B (1998)347.

[37] A. Akindinov et al., NIM, A494 (2002) 474.

[38] G.Bondarenko et al., NIM, A442 (2000) 187.

[39] V.Golovin, V.Saveliev, NIM, A518 (2004) 560.